NEGATIVE GROUP VELOCITY OF ULTRASONIC PULSES IN A BUBBLY LIQUID

DEL M. LEARY

Negative group velocity of ultrasonic pulses in a bubbly liquid

by

Del M. Leary

A THESIS SUBMITTED TO THE

SCHOOL OF GRADUATE STUDIES

IN PARTIAL FULFILLMENT

OF THE REQUIREMENTS

FOR THE DEGREE OF

MASTER OF SCIENCE

DEPARTMENT OF PHYSICS AND PHYSICAL OCEANOGRAPHY

MEMORIAL UNIVERSITY OF NEWFOUNDLAND

JUNE 2001

ST JOHN'S NEWFOUNDLAND

Abstract

A wave pulse can propagate with a negative group velocity when it travels through a medium with anomalous dispersion, that is, when the derivative of the dispersion curve is negative. Here we report on the experimental observation of negative group velocities for pulses of ultrasound propagating ballistically through water containing gas bubbles. For frequencies near the resonant frequency of the bubbles, the absorption increases strongly and the group velocity becomes negative. Our experimental results are in good agreement with a theoretical model sound propagation in bubbly liquids if we assume a Gaussian distribution of bubble sizes.

Acknowledgements

I would like to thank John de Bruyn for the opportunity to undertake such a special project. Your support and understanding has strengthened me as a student and as a person. I would also like to thank my collaborators John Page and Mike Cowan for their patience and wisdom, and the University of Manitoba where the ultrasonic experiments were performed. I also have to re-thank past mentors Gabor Kunstatter and Randy Kobes for seeing potential in me, and giving me an opportunity. I have to thank Dwight Vincent for his inspiration.

I would like to thank my entire family, my parents Cam and Christine for their everlasting support and guidance, also my brothers Trav and Keith for being who they are. I couldn't have done it without you. I would like to thank Grandma, Helen, Ted, Ed and family, and of course, my Grandpa for his faith and perception towards all living things.

My friends are the most amazing group of people I could ever meet. You have kept me real. To Kelly, to whom this body of work mattered the least, but gave the most.

I want to give my utmost thanks to the people I have met in Newfoundland. You have made a second home for me here. To neighbors Chuck and Jenny, your kindness and friendly smiles will not be forgotten. I would love to thank you all individually, and will in time. This closes a truly great chapter my life.

Contents

List of Figures

List of Tables

1 Introduction

On any given day, our perception of and interaction with the world is made possible due to energy transmitted in the form of waves. Waves come in many different forms: for example, and sound in the form of acoustic waves, and radio and light in the form of electromagnetic waves [1]. Using classical wave theory, we can characterize waves by their dispersion curves (the angular frequency ω as a function of the wavenumber k), which give us information about the frequency (or wavelength) and propagation speed of the waves. The frequency of light determines its color, whereas the frequency of sound determines the pitch or tone of the sound one hears. When we change the length of a musical device, a penny whistle for example, we are changing the wavelength of the sound produced. The change in wavelength changes the frequency, and therefore the pitch that we hear from the instrument. However, this example is rather trivial, and the relationship between frequency and wavelength is not always so simple. If the speed is independent of frequency then the dispersion curve is linear, so $\omega \propto k$ or $f \propto 1/\lambda$. However, if the speed is not constant as a function of frequency, then a change in wavelength does not always lead to a proportional change in frequency, and vice versa. Depending on the substance through which a wave is propagating, the dispersion relation can be very complicated and interesting.

This thesis is focused on measurements of the propagation of ultrasound through a bubbly liquid, but the physics behind it shares a commonality with that of many other

systems, involving many types of waves. In particular we mainly look at ballistic propagation, in which the sound wave is either unscattered or forward-scattered as it propagates through the medium.

The quantities measured are attenuation, extinction length, phase velocity, and group velocity. A pulse is sent through a sample (in this case bubbles in liquid) and the ballistic properties can be determined by examining the wave pulse after it leaves the sample. The attenuation tells us how much the wave has decayed in intensity due to its interaction with the sample. The extinction length, the inverse of the attenuation, tells us how far the wave has traveled before being either scattered or absorbed. The phase velocity is the velocity of a sinusoidal 'carrier' wave, defined in terms of the dispersion curve as $V_p = \omega/k$.

The amplitude of a wave pulse varies in time. This amplitude variation is necessary if we wish to convey information from one place to another. There are several ways of defining the velocities of a wave packet. These include group, signal and energy velocity [2]. *Group velocity* is defined as the propagation speed of the peak of a wave packet. Stated another way, the group velocity is the distance traveled by the peak of the wave packet divided by the time it takes to travel that distance. We can find the group velocity from the dispersion curve by taking its derivative (or slope), $V_g = \partial\omega/\partial k$. In some cases, when the medium is anomalously dispersive the group velocity can become negative. *Signal velocity* is measured using the infinitesimal onset of the packet rather than the peak. This has obvious impracticalities since the detection of the first sign of the wave

packet is limited experimentally and would differ depending on sensitivity, pulse width, amplitude etc. Brillouin himself expresses some concerns: "In general the signal velocity measured depends on the sensitivity of the detecting apparatus used. With a very sensitive detector, even the forerunners, or certain parts of them, might be detected... But if the sensitivity of the detector is restricted to a quarter or half the final signal intensity, then an unambiguous definition of the signal velocity can, in general be given" [2]. The *energy velocity* is defined as the ratio between the energy flux and the energy density. Measurement of the energy velocity does not suffer from the shortcomings of the group and signal velocities, which also measure the speed of information transport.

1.1 History

Although the origin of wave theory is hard to determine accurately, the last few centuries have seen many contributions to what we would call modern wave mechanics. Isaac Newton provided the mathematical vigor for Brook Taylor's earlier work on matching his vibrating string theory to that of experimental observations. This in turn allowed the derivation of the general wave equation by the French scientist Jean Le Rond. Later Jean-Baptiste-Joseph Fourier created the theory of dividing the complex periodic wave into its spectral components, today known as the Fourier transform. The mark of modern acoustics was thought to come with the publication of the *Theory of Sound* in 1877 by Lord Rayleigh. Although scientists such as LeConte, Tyndall, and the

Curie brothers initiated the study of Ultrasonics in the 19th century, detailed analysis could not be achieved until the early 20th century.

Sommerfeld and Brillouin showed that if a wave packet travels through a medium that is highly absorptive, a phenomenon known as anomalous dispersion could occur. Brillouin states, "... but if absorption also occurs, a [the wave vector] becomes complex or imaginary and the group velocity ceases to have a clear physical meaning"[3]. This was further confirmed by J. D. Jackson in his well-respected book *Classical Electrodynamics* [4]. Also, Landau and Lifshitz write, "When considerable absorption occurs, the group velocity cannot be used, since in absorbing medium wave packets are not propagated but rapidly ironed out" [5].

1.2 Background

The theoretical model used in this thesis comes from the work of Prosperetti [6]. The model describes the response of a gas bubble when subjected to the changes of pressure due to an incident ultrasonic wave. The behavior of the bubble is that of a damped harmonic oscillator.

There has not been much experimental work on the ballistic propagation of waves through water containing bubbles since the work done in the 1950s by Fox et al[7] who

took ballistic measurements of air bubbles. This work did not focus on the phenomenon of anomalous dispersion that can be found in bubbly liquids. The present work is the first detailed study of negative group velocities using ultrasonic waves in liquid media. Other work, mostly on light waves, has found that in anomalous dispersive situations superluminal and negative group velocity does occur [8, 9]. Other forms of waves have also shown negative group velocities under certain conditions[10]. Often these works compare group velocity with other methods of information transfer, using energy or signal velocities [11]. The energy and signal velocity measurements do not break causality. Although the negative group velocities would indicate super-luminal velocities, this effect is caused by pulse reshaping due to the anomalous dispersion and causality is never violated. This thereby reassures us that no information can travel faster than the speed of light.

In our experiment we generated bubbles with a measured size distribution within a liquid and sent in ultrasonic pulses with frequencies at and near the resonant frequency of the bubbles. By looking at the coherent component of the output pulses, we were able to obtain very accurate ballistic measurements. Of particular interest was the group velocity. We measured the group velocity as a function of frequency and found that for large enough bubble concentrations, the group velocity becomes negative at resonance.

1.3 Thesis Outline

The remainder of this thesis is organized as follows. Chapter Two deals with the theory. We explain the resonance and damping nature of an individual bubble in an acoustic field, expressed in analogy to a driven damped harmonic oscillator. We then find the attenuation and signal velocity by determining the complex wavenumber for a given concentration and size distribution of bubbles. The theoretical group velocity is calculated directly from the phase velocity. In Chapter Three we describe the experimental set-up. Chapter Four briefly describes the bubble generation and image techniques and the way in which the bubble size distribution is determined experimentally. A results chapter follows in which the details of the data analysis are given along with the experimental results. The experimental results are compared with the theoretical model. The results are then discussed in the final chapter.

2 Theory

2.1 Introduction

The theoretical background for our experiments will be formulated in this chapter. We begin with a derivation of the resonant frequency and damping coefficients of a single bubble in Sec. 2.2. We describe the cross-sections for acoustic scattering and absorption in Sec. 2.3 to better understand the attenuation in our medium as a function of frequency. In Sec. 2.4 we give a formulation of the complex wave vector for the bubbly medium. From the wave vector we can find the phase velocity and attenuation as a function of frequency. In Sec. 2.5, we derive the theoretical group velocity from the phase velocity.

2.2 Resonant Frequency and Damping

A sound wave propagating through a medium consisting of bubbles in a liquid will excite oscillations of the bubbles. We start by examining a single bubble in equilibrium. We then consider a bubble oscillating harmonically in response to being driven at some frequency. This will lead to expressions for the resonant frequency of the bubble as a function of bubble radius, and for the damping of the oscillations due to viscous, thermal, and radiative processes. Our analysis is based on that in Ref [12].

We first identify the contributions to the pressure inside and outside the bubble. Inside the bubble we have the pressure of the gas, p_g, and the pressure due to water vapor, p_v. The pressure outside the bubble is the sum of the surface tension pressure, p_σ, and the pressure of the surrounding fluid just outside the bubble, p_L. In equilibrium, the pressure outside the bubble balances the pressure inside. Thus the pressure inside the bubble, p_i, can be expressed as

$$p_i = p_g + p_v = p_L + p_\sigma. \tag{2.1}$$

When the bubble is driven by sound at an angular frequency ω, the bubble radius can change. Neglecting the viscosity of the gas, the external pressure then includes a viscous drag term, so Eq. (2.1) becomes

$$p_i = p_L + p_\sigma + \frac{4\eta\dot{R}}{R}, \tag{2.2}$$

where η is the liquid viscosity, R is the radius of the bubble, and the dot indicates the time derivative. The first two terms on the right-hand side of Eq.(2.2) are given by

$$p_\sigma = \frac{2\sigma}{R}, \tag{2.3}$$

and

$$p_L = p_0 + P_A e^{i\omega t} + P_{bl}(r = R_0), \tag{2.4}$$

where σ is the surface tension and R_0 is the equilibrium bubble radius. The hydrostatic pressure p_0 is defined as

$$p_0 = P_{atm} + hg\rho_0 \tag{2.5}$$

where P_{atm} is the atmospheric pressure, h is the distance from the surface of the liquid, g is the acceleration due to gravity, and ρ_0 is the equilibrium fluid density. The term $P_A e^{i\omega t}$ is the pressure contribution due to the incident sound wave. The final term in Eq. (2.4) is the acoustic pressure field radiated away by the bubble, evaluated at the equilibrium position of the bubble wall. Prosperetti [6] finds P_{bl} from the velocity potential for the fluid around a pulsating bubble:

$$\Phi(r,t) = -\frac{\rho_0 R_0^2 \dot{R}}{r\left(1 + i\omega R_0 / c\right)} e^{-ik(r-R_0)}, \tag{2.6}$$

as given by Landau and Lifshitz [13] for the case when viscous terms are negligible. Here, c is the speed of sound in the pure liquid, and r is the radial coordinate measured from the center of the bubble. Eq. (2.6) is substituted into the general equation for the acoustic pressure,

$$P_{bl} = -\rho_0 \dot{\Phi}, \tag{2.7}$$

and evaluated at $r = R_0$. When the result is substituted into Eq. (2.4), we arrive at

$$p_L = p_0 + P_A e^{i\omega t} + \frac{\rho R_0 \ddot{R}}{1 + i\omega R_0 / c}. \tag{2.8}$$

For small amplitude oscillations, we can write $R = R_0 + R_\varepsilon$, where $R_\varepsilon \ll R_0$. Such oscillations will produce small amplitude perturbations p_ε from the equilibrium internal bubble pressure $p_{i,e}$. This is expressed as

$$p_i = p_{i,e} + p_\varepsilon(t). \tag{2.9}$$

Substituting Eqs. (2.8) and (2.9) into Eq. (2.2) we arrive at the equation

$$p_{i,e} + p_\varepsilon(t) = p_0 + P_A e^{i\omega t} + \frac{\rho R_0 \ddot{R}}{1 + i\omega R_0 / c} + \frac{2\sigma}{R} + \frac{4\eta \dot{R}}{R}. \tag{2.10}$$

Regrouping the above equation and using the fact that $p_{i,e}$ is equal to the hydrostatic pressure p_0, we get

$$\frac{\rho R_0^2}{1+i\omega R_0/c}\left[\frac{\ddot{R}_\varepsilon}{R_0}\right]+4\eta\left[\frac{\dot{R}_\varepsilon}{R_0}\right]-\frac{2\sigma}{R_0}\left[\frac{R_\varepsilon}{R_0}\right]=p_\varepsilon-P_A e^{i\omega t}. \tag{2.11}$$

The form of p_ε has been derived by Prosperetti [6]. Details of the derivation can be found in Ref. [1] (p.371). The result is

$$p_\varepsilon=3\kappa p_{i,e}\left[\frac{R_\varepsilon}{R_0}\right]-4\eta_{th}\left[\frac{\dot{R}_\varepsilon}{R_0}\right], \tag{2.12}$$

where κ is the polytropic index[1], and η_{th} is an additional thermal contribution to the effective viscosity. Substituting Eq. (2.12) into Eq. (2.11), we arrive at

$$\begin{aligned}&(\rho R_0)\left[\ddot{R}_\varepsilon\right]+(\rho R_0)\left(4\frac{\eta+\eta_{th}}{\rho R_0^2}+\omega\frac{\omega R_0/c}{1+(\omega R_0/c)^2}\right)\left[\dot{R}_\varepsilon\right]\\&+(\rho R_0)\left(\frac{3\kappa p_{i,e}}{\rho R_0^2}-\frac{2\sigma}{\rho R_0^3}+\frac{\omega^2(\omega R_0/c)^2}{1+(\omega R_0/c)^2}\right)\left[R_\varepsilon\right]=-P_A e^{i\omega t},\end{aligned} \tag{2.13}$$

which is the equation for a damped harmonic oscillator. The effective "spring constant", or stiffness of the system is

$$k=(\rho R_0)\left(\frac{3\kappa p_{i,e}}{\rho R_0^2}-\frac{2\sigma}{\rho R_0^3}+\frac{\omega^2(\omega R_0/c)^2}{1+(\omega R_0/c)^2}\right). \tag{2.14}$$

The ratio of this to the effective mass $m=\rho R_0$, gives

$$\omega_0^2=\frac{k}{m}=\left(\frac{3\kappa p_{i,e}}{\rho R_0^2}-\frac{2\sigma}{\rho R_0^3}+\frac{\omega^2(\omega R_0/c)^2}{1+(\omega R_0/c)^2}\right), \tag{2.15}$$

which is the square of the resonant frequency.

---

[1] The polytropic index is the exponent describing the family of curves pV^κ = constant. These curves describe systems that are neither perfectly isothermal, nor perfectly adiabatic.

If we look at the damping term in Eq. (2.13) we can identify contributions to the dissipation due to thermal, radiation, and viscous damping. The corresponding damping terms are

$$b_{th} = \frac{4\eta_{th}}{R_0}, \tag{2.16}$$

$$b_{rad} = (\rho\omega R_0)\left(\frac{\omega R_0/c}{1+(\omega R_0/c)^2}\right), \tag{2.17}$$

and

$$b_{vis} = \frac{4\eta}{R_0}, \tag{2.18}$$

respectively. The total damping is simply the sum of these,

$$b_{tot} = b_{th} + b_{rad} + b_{vis}. \tag{2.19}$$

We can non-dimensionalize these to get the dimensionless damping terms

$$d_{th} = \frac{\omega b^{th}}{k} = \frac{4\eta_{th}}{R_0}\frac{\omega}{\rho R_0}\left(\frac{3\kappa p_{i,e}}{\rho R_0^2} - \frac{2\sigma}{\rho R_0^3} + \frac{\omega^2(\omega R_0/c)^2}{1+(\omega R_0/c)^2}\right)^{-1}, \tag{2.20}$$

$$d_{rad} = \frac{\omega b_{rad}}{k} = \omega^2\left(\frac{\omega R_0/c}{1+(\omega R_0/c)^2}\right)\left(\frac{3\kappa p_{i,e}}{\rho R_0^2} - \frac{2\sigma}{\rho R_0^3} + \frac{\omega^2(\omega R_0/c)^2}{1+(\omega R_0/c)^2}\right)^{-1}, \tag{2.21}$$

and

$$d_{vis} = \frac{\omega b_{vis}}{k} = \frac{4\eta}{R_0}\frac{\omega}{\rho R_0}\left(\frac{3\kappa p_{i,e}}{\rho R_0^2} - \frac{2\sigma}{\rho R_0^3} + \frac{\omega^2(\omega R_0/c)^2}{1+(\omega R_0/c)^2}\right)^{-1} \tag{2.22}$$

The total dimensionless damping is sum of these,

$$d_{tot} = d_{th} + d_{rad} + d_{vis}. \tag{2.23}$$

The dimensionless damping terms are plotted as a function of frequency for a particular bubble radius in Fig. 2.1. At low frequencies, the damping is mostly due to the thermal contribution. As frequency increases, the radiative damping constant becomes dominant.

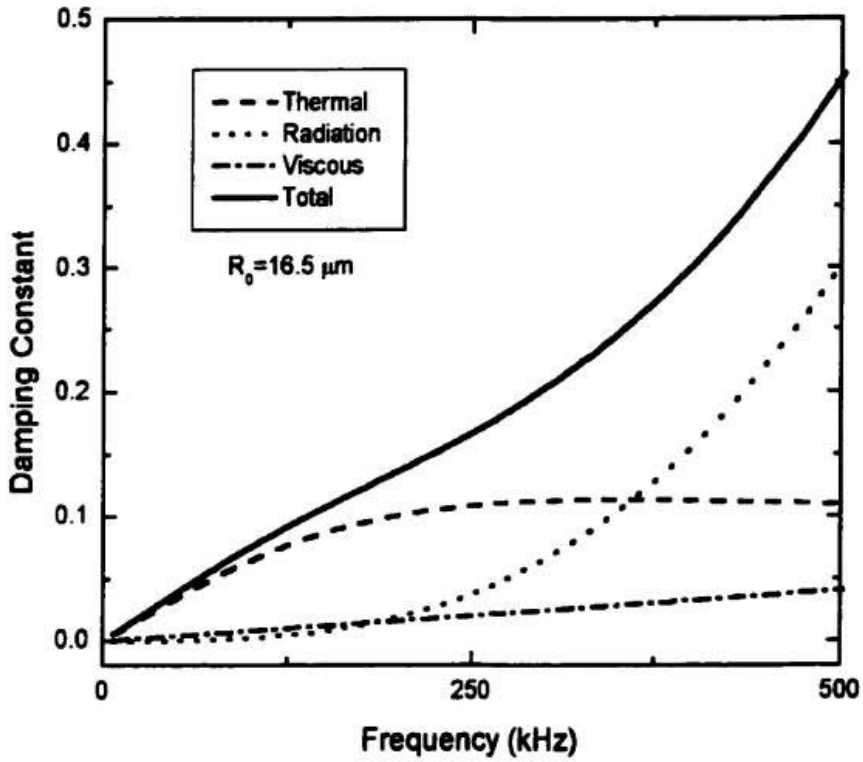

Figure: 2.1

The dimensionless damping due to thermal, viscous, and radiative damping as a function of frequency for a bubble of radius of 16.5 microns. The total damping constant is also shown.

2.3 The Absorption and Scattering Cross-sections

The loss of energy from an incident wave can be characterized by assigning an extinction cross-section σ_{ext} to the bubble. The cross-section is defined as the ratio of the time averaged power subtracted from the sound wave as a result of the presence of the bubble, to the intensity of the beam. The extinction cross-section is the sum of contributions from both the scattering σ_s and absorption σ_a cross-sections,

$$\sigma_{ext} = \sigma_s + \sigma_a \tag{2.24}$$

The time-average rate at which energy from the plane wave is re-radiated by the *scattering* bubble is

$$\omega^2 |A|^2 b_{rad} / 2, \tag{2.25}$$

where A is the amplitude of the oscillation. The plane wave intensity

$$I = P_A^2 / (2\rho c) \tag{2.26}$$

is the square of acoustic pressure amplitude, P_A, divided by two times the impedance ρc. Therefore, the scattering cross-section can be written as

$$\sigma_s = \frac{\omega^2 |A|^2 b_{rad} \rho c}{P_A^2}. \tag{2.27}$$

Leighton [12](p.296) has shown Eq. (2.27) to be equal to

$$\sigma_s = \frac{4\pi Ro^2}{\left((\omega_0/\omega)^2 - 1\right)^2 + \left(\frac{b_{tot}}{\omega 4\pi Ro^3 \rho}\right)}. \tag{2.28}$$

The *absorption* cross-section will include damping from both viscous and thermal contributions. We can find this value by dividing out the radiative damping from Eq. (2.27) and multiplying by the sum of the viscous and thermal damping. We then have

$$\sigma_a = \frac{b_{th} + b_{vis}}{b_{rad}} \sigma_s. \tag{2.29}$$

These cross-sections are frequency and bubble-size dependant, and at resonance can be hundreds to many thousands the size of the bubble's geometric cross-section depending on the amount of damping in the medium. We can see how the cross-sections depend on frequency in Fig. 2.2 where they are plotted for a bubble size of 16.5 microns. Fig. 2.2 shows that at resonance the attenuation is mainly due to absorption. The cross-sections cross over at about 0.39 MHz, where the scattering cross-section becomes greater. The geometric cross-section for a 16.5 micron bubble is ~0.0009 mm^2, approximately 10^{-3} times the acoustic cross-sections.

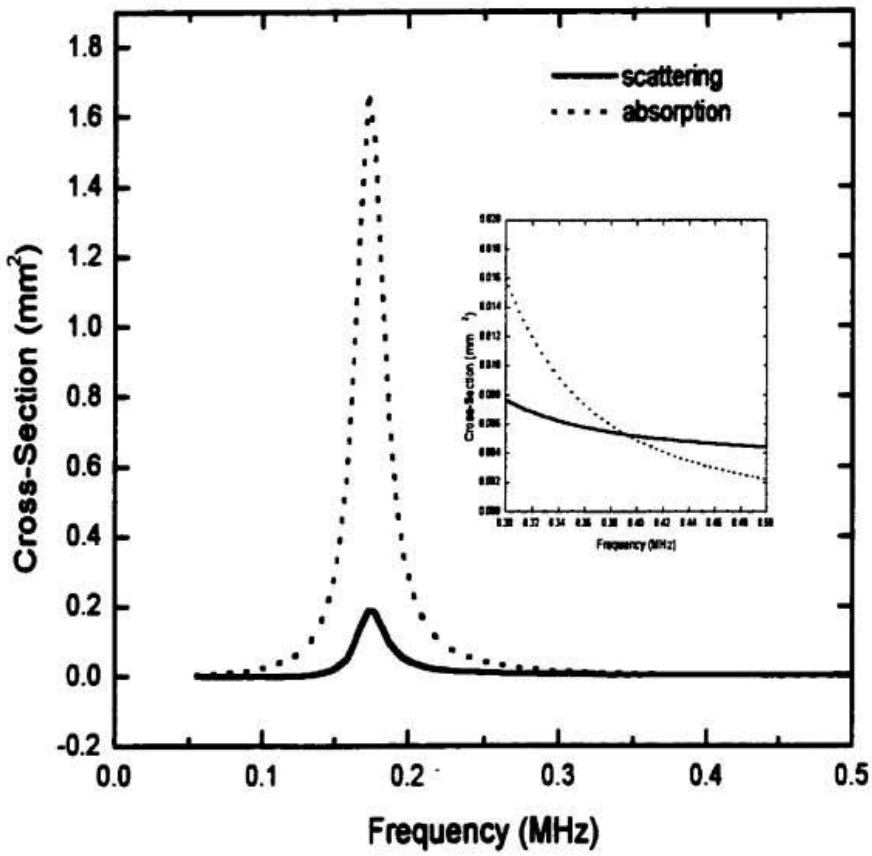

Figure: 2.2

The absorption and scattering cross-sections for a bubble radius of 16.5 microns. At resonance, the absorption cross-section is much greater than the scattering cross-section. The inset shows that above resonance, scattering becomes greater than absorption.

2.4 Phase velocity and attenuation.

There have been a number of theoretical calculations of the phase velocity of sound in dispersive media [7, 14]. The different calculations agree quite well with one another. Here we follow the calculation given by Leighton [12]. The speed of sound, c_c (where the subscript c indicates the mixed gas/liquid medium), is defined as

$$c_c = \sqrt{\frac{B_c}{\rho_c}}, \tag{2.30}$$

where B_c and ρ_c are the bulk modulus and the density of the medium respectively. Since the density does not vary dramatically, the bulk modulus is responsible for most of the variation in the speed of sound in the medium. The bulk modulus is defined as

$$B = -V\left(\frac{dp}{dV}\right), \tag{2.31}$$

where V is the volume and p the pressure.

In our medium, the total bulk modulus is related[2] to that for the bubbles plus that for the liquid:

$$\frac{1}{B_c} = \frac{1}{B_w} + \frac{1}{B_{bub}}. \tag{2.32}$$

B_w is simply given by

$$B_w = c_w^2 \rho_w, \tag{2.33}$$

where c_w is the speed of sound in water and ρ_w is the density of water.

To calculate B_{bub}, we start by considering how one bubble responds to a pressure change, then sum over all bubbles. Consider a population of n_b identical bubbles per unit volume, each bubble having volume $V_1(t)$. When the entire population is affected by a pressure change, the resulting bulk modulus is

$$B_{bub} = -\frac{1}{n_b \Delta V_1} \Delta p. \tag{2.34}$$

If the radius of the bubble is perturbed as in the previous section, then

$$V_1(t) = \frac{4\pi R(t)^3}{3} = \frac{4\pi R_0^3}{3}\left(1+\frac{R_\varepsilon}{R_0}\right)^3 \approx V_0\left(1+\frac{3R_\varepsilon}{R_0}\right)$$

for small amplitude linear oscillations ($R_\varepsilon \ll R_0$). Here V_0 is the volume of the bubble in equilibrium. Letting $\Delta V_1(t)$ be the perturbation to the volume, we have

$$V_1(t) = V_0 + \Delta V_1(t) \approx V_0 + \frac{3V_0 R_\varepsilon}{R_0},$$

so

$$\Delta V_1(t) \approx \frac{3V_0 R_\varepsilon}{R_0}. \tag{2.35}$$

Substituting this into Eq. (2.34), we find the bulk modulus due to the bubbles to be

$$B_{bub} = -\frac{R_0 \Delta p}{3n_b V_0 R_\varepsilon}. \tag{2.36}$$

---

[2] It should be noted that in Leighton (p.299) that the total bulk modulus is given as the sum, $B_c = B_{bub} + B_w$. This relation is incorrect and was possibly confused with the relation $k_c = k_{bub} + k_w$, where k is the compressibility and is defined as $k = 1/B$.

The perturbed radius is found by solving the general damped harmonic oscillator relation, using

$$\ddot{R}_\varepsilon + 2\beta\dot{R}_\varepsilon + \omega_0^2 R_\varepsilon = \frac{F_0}{m}e^{i\omega t} \tag{2.37}$$

where $\beta = b_{tot}/2m$, $F_0 = -P_A 4\pi R_0^2$, and P_A is the acoustic pressure amplitude.

The result is

$$R_\varepsilon = -\frac{P_A e^{i\omega t}}{R_0\rho_w}\frac{1}{((\omega_0^2-\omega^2)+i2\beta\omega)}. \tag{2.38}$$

Noting that $\Delta p = -P_A e^{i\omega t}$, and substituting Eq. (2.38) into Eq. (2.36) we arrive at

$$B_{bub} = \frac{R_0^2\rho_W((\omega_0^2-\omega^2)+i2\beta\omega)}{3n_b V_0}. \tag{2.39}$$

Note that B_{bub} is complex, so our final sound speed will also be complex. The complex wavenumber of the sound wave is

$$k_c^{comp} = \frac{\omega}{c_c} = \omega\sqrt{\frac{\rho_c}{B_c}}. \tag{2.40}$$

Assuming that the total volume fraction of the bubbles is small, so that $\rho_c \approx \rho_w$, we can rearrange Eq. (2.40) to get

$$k_c^{comp} \approx \frac{\omega}{c_w}\sqrt{1+\frac{c_w^2\rho_w}{B_{bub}}}. \tag{2.41}$$

Using B_{bub} from Eq. (2.39) with $V_0 = 4\pi R_0^3/3$ gives

$$k_c^{comp} \approx \frac{\omega}{c_w}\sqrt{1+\frac{4\pi n_b c_w^2 R_0}{((\omega_0^2-\omega^2)+i2\beta\omega)}}. \tag{2.42}$$

From the real part of the wavenumber, we can determine the phase velocity of the propagating wave:

$$V_p = \frac{\omega}{\mathrm{Re}\left(k_c^{comp}\right)}. \tag{2.43}$$

Fig 2.3 shows the calculated phase velocity in a bubbly medium containing 17 million bubbles per cubic meter. The bubbles had a radius of 15 microns.

While from the imaginary part of the wavenumber, we can determine the attenuation,

$$\alpha = -2\,\mathrm{Im}\left(k_c^{comp}\right). \tag{2.44}$$

Because in Eq. (2.44) we are calculating the intensity attenuation, we include a factor of two. A theoretical plot of the attenuation, for the same medium used for the phase velocity, is given in Fig. 2.4.

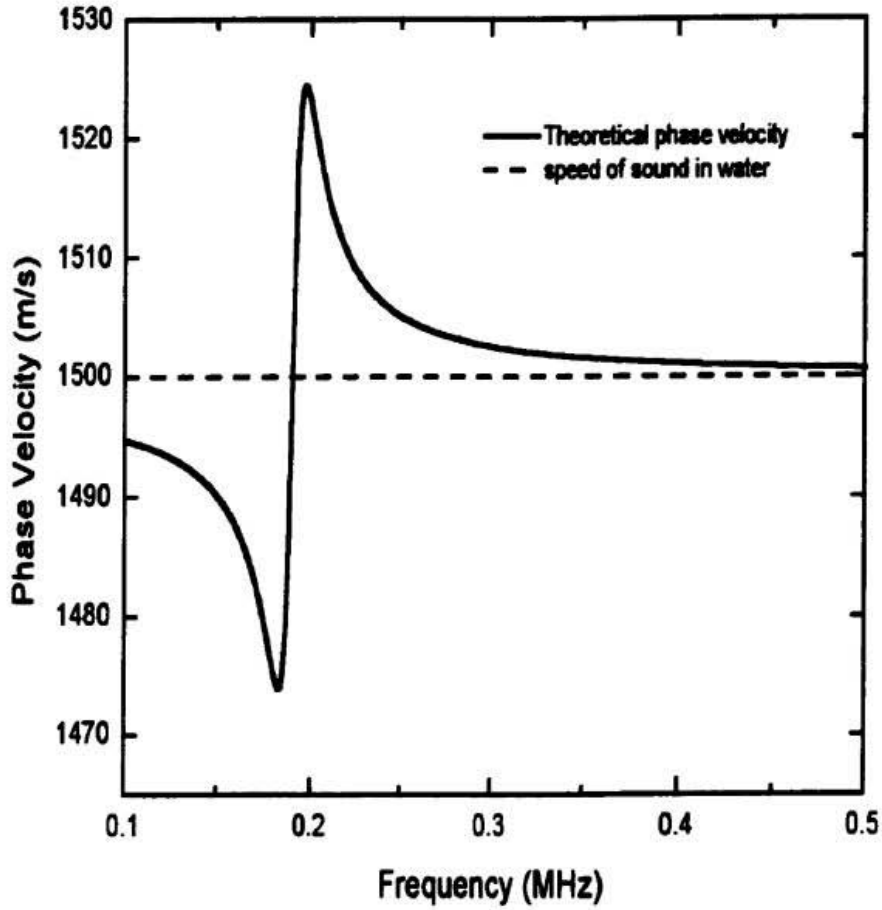

Figure: 2.3

The theoretical phase velocity for a bubbly liquid containing a single bubble radius of 15 microns. The concentration is 17 million bubbles per cubic meter, which is typical for our experiments. The speed in pure water is 1500 meters per second.

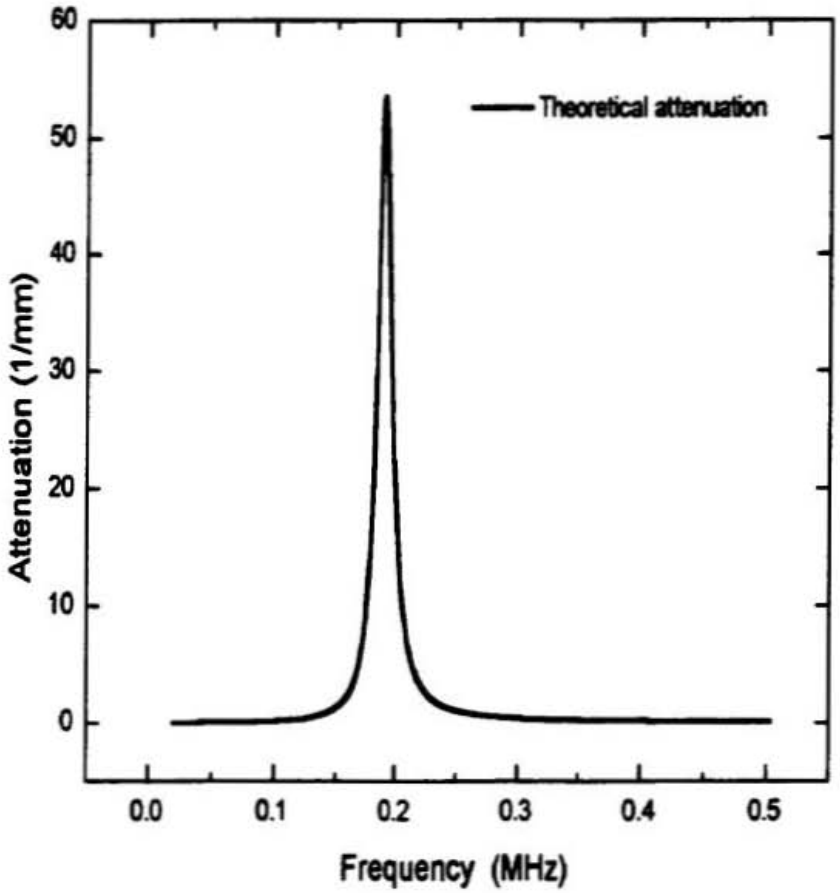

Figure: 2.4

The theoretical attenuation for a bubbly liquid with 17 million bubbles per cubic meter, each of radius 15 microns. The resonant frequency of the bubbles is ~0.188 MHz.

2.5 Group velocity

The group velocity was determined from the theoretical phase velocity in the following way. First from the definitions of V_p and V_g we have,

$$V_p = \frac{\omega}{k}; V_g = \frac{d\omega}{dk}. \tag{2.45}$$

We can then say,

$$V_g = \frac{d\omega}{d\left(\omega / V_p\right)}. \tag{2.46}$$

By finding k from the phase velocity, we could then numerically solve for the group velocity. An example for this is given in Fig. 2.5 for a medium containing 17 million bubbles per cubic meter each having a bubble radius of 15 microns.

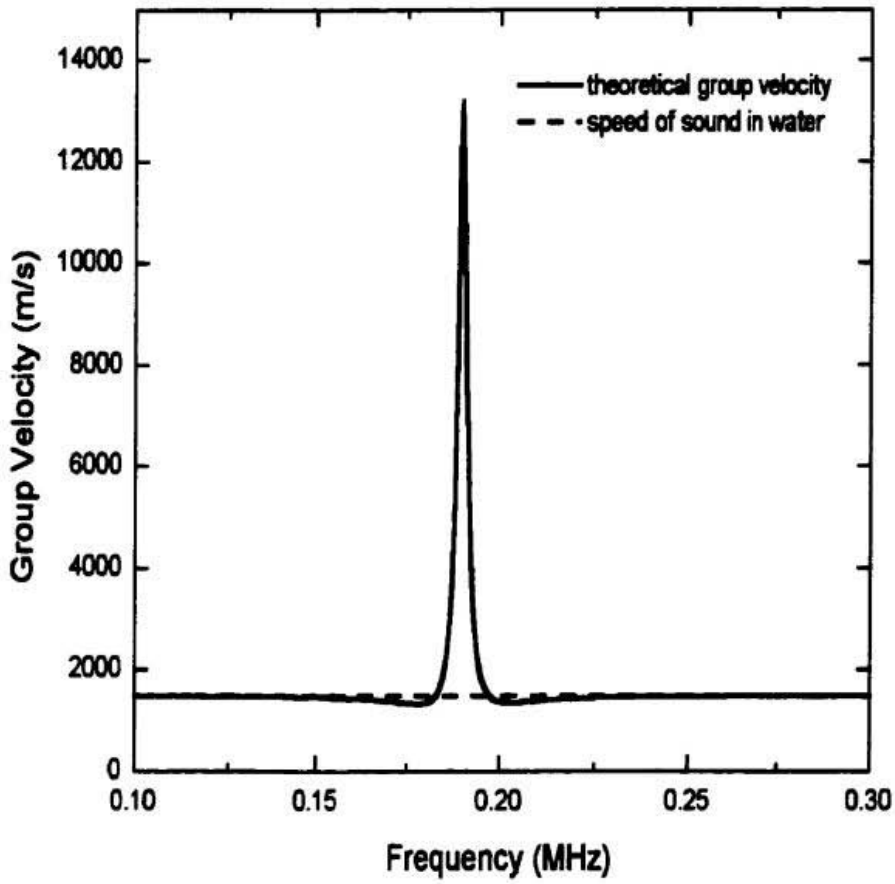

Figure: 2.5

The theoretical group velocity for a bubbly liquid with a concentration of 17 million bubbles per cubic meter, consisting of bubbles having a single bubble radius of 15 microns. The dotted line shows the speed of sound in pure bubble free water.

3 Experimental Setup and Apparatus.

3.1 Setup

The ballistic measurements were designed to detect the unscattered or forward-scattered components of an ultrasonic pulse that has traveled through the sample.

A block diagram of the experimental apparatus for the ballistic measurements is given in Fig 3.1. All measurements were done in a 425-liter glass tank (1.2 m x 0.6 m x 0.6 m) filled with water. The water provided a convenient coupling medium for the ultrasonic waves. Without it, high impedance mismatches would lead to energy loss from reflections and make the experiments impossible. This tank contained the sample cell, which was placed in the far field of the generating and receiving transducers. The walls and floor of the tank were lined with 2.5-cm-thick Styrofoam insulation to reduce reflections. Additional parallel strips of Styrofoam ribbing placed 10 cm apart along the walls further reduced reflections. Surrounding the tank was a steel frame that supported mounts for the sample and transducers.

Motorized translation stages were used to simply and accurately set the position of the sample and transducers. The stepper-motor translation stages were Unislide™ positioning systems manufactured by Velmex, Inc. (East Bloomfield, NY). They could move in increments of 3.175 μm, over a 30 cm range. These stages were mounted on a supporting cradle that allowed for three dimensional position adjustments.

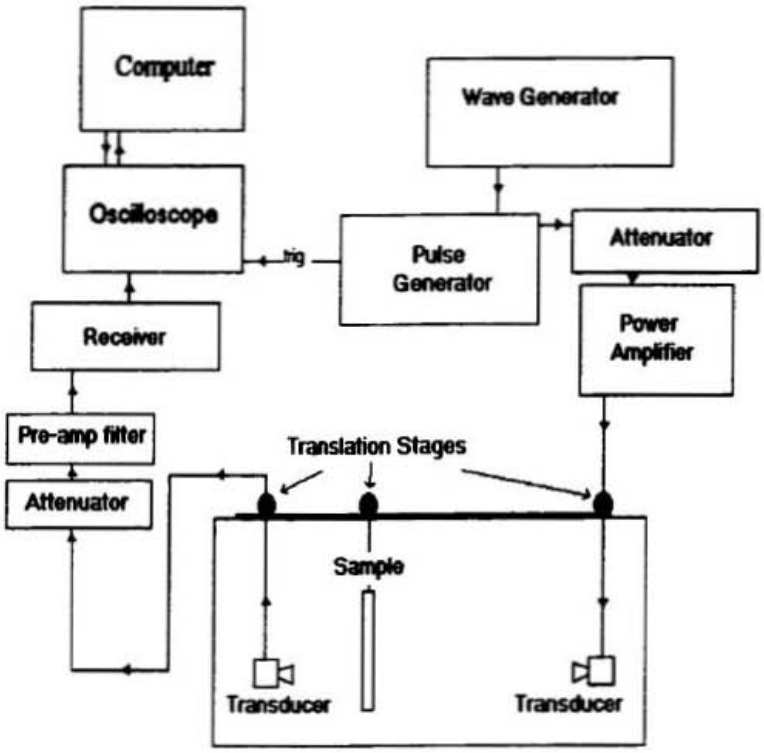

Figure: 3.1
Block diagram of the ballistic setup.

Two different signal generators were used. The first and most reliable was a Fluke model 6060B synthesised RF signal generator (John Fluke Mfg. Co., Everett, Washington). This device was operated at 13 dBm. When this generator was unavailable, it was replaced by a GW model GFG-8016G (Good Will Instrument Co. Ltd, Malaysia). The continuous sine wave signal from the generator was mixed (i.e., multiplied) with a rectangular pulse, by triple cascading MiniCircuits model 15542 ZAY-

3 mixers. The result was a sine wave 'pulse' controlled by the pulse generator, a Stanford Research Systems Inc. (Sunnyvale, CA) model DG535 digital delay/pulse generator that provided very precise time delay. Pulse widths of 2 to 50 μs were used, depending on the signal frequency and the measurement being performed. The pulse repetition period ranged from 5 to 30 ms. The resulting low power rectangular RF pulse was then fed through a Telonic Altair model 8143A, 50 ohm attenuator, and then into a model 250L Amplifier Research (Souderton, PA) power amplifier, which had a peak output power of 250 watts.

The plane wave transducers that were used were Accuscan-V series immersion transducers from Panametrics, Inc. (Waltham, MA). Transducers with central frequencies of 0.1, 0.25, 0.5, 1.0, 2.25 MHz were used so that a large range of frequencies could be studied. The 0.1 MHz and 0.25 MHz transducers had a diameter of 3.81 cm, slightly larger than the 2.54 cm. diameter of higher frequency transducers. To obtain a plane wave signal at the sample, the transducer was used in the far field. The distance from the generating transducer to the sample z, had to be greater that z_f, given by

$$z_f = \frac{R^2}{\lambda}. \tag{3.1}$$

This distance z_f defines the transition between the near and far field, or Fresnel and Fraunhofer zones. Here R is the radius of the transducer and λ the wavelength generated.

The signal received by the detector was fed through a second attenuator and into a pre-amp system, either a model 253 Matec broadband pre-amp providing 20 dB of gain, or a model 252 Matec double tuned pre-amp providing approximately 30 dB of gain. The signal was then fed into a model 605 Matec (Hopkinton, MA) broadband receiver. This system not only amplified the very weak signal but could also filter the pulse shape and central frequency (for the tuned case only).

A Tektronix model TDS 544A (Beaverton, OR) oscilloscope was used to acquire digitized signals of both reference and sample pulses. The sample rate was generally set at 10 MS/s. For ballistic measurements the oscilloscope would average 10 000 readings, effectively averaging out the scattered component of the signal. Digitized data were sent to a personal computer via an IEEE bus.

4 The Scattering Medium

4.1 Introduction

An important part of this work was the design of the cell and the bubble generating process. The idea was to create bubbles with a narrow size distribution that move randomly with respect to one another. We wanted to generate rather small bubbles (~15 microns in radius) to get the resonant frequencies in the desired range (~200 kHz). The bubble distribution also had to be reproducible from day to day. The geometry of the cell was arranged to produce a region where the mean flow was small, leading to an area with random bubble motion. The bubbles were generated by hydrolysis of a solution of 1% Na_2SO_4 and 1% Sodium dodecyl sulfate (SDS) by weight in distilled water. The electrodes were made of platinum, and electrolysis currents ranging from 10mA to 50mA were used. The bubble concentrations and size distributions were determined by taking pictures of the medium with a video microscope, then analyzing the pictures using imaging software.

4.2 Cell Design

Figure 4.1 is a diagram of the cell. It was rectangular in shape and had internal structures consisting of two guiding barriers to direct the flow of the bubbles and two electrodes. The cell had a height of 21.6 cm, a width of 22.2 cm, and a thickness of 4.5 mm. Nearly the entire cell including the frame, barriers, and walls of the cell were made of Plexiglas and other versions of PMMA (polymethyl methacrylate). Ideally, the cell materials should have a small effect on the propagating wave. However, reflections within and between the cell walls were found to have a visible effect on our data as described in Chap.5.

Bubbles were generated using hydrolysis. The cathode generated hydrogen bubbles and the anode produced oxygen bubbles. The hydrogen bubbles were used in the experiments because they were smaller than the oxygen bubbles. In addition, the overall hydrogen production rate was twice the oxygen production rate, so we could achieve higher bubble concentrations at lower electrical currents using the hydrogen bubbles. The internal construction of the cell separated the different gas bubbles. The oxygen bubbles were guided up the side of the wall then vented, while the hydrogen bubbles were led into the sample area. To achieve a narrow distribution of bubble sizes we used the ideas of Stokes' velocity law [12], which states that the velocity of the rising bubble is proportional to the square of its radius. The larger bubbles quickly rose to the surface,

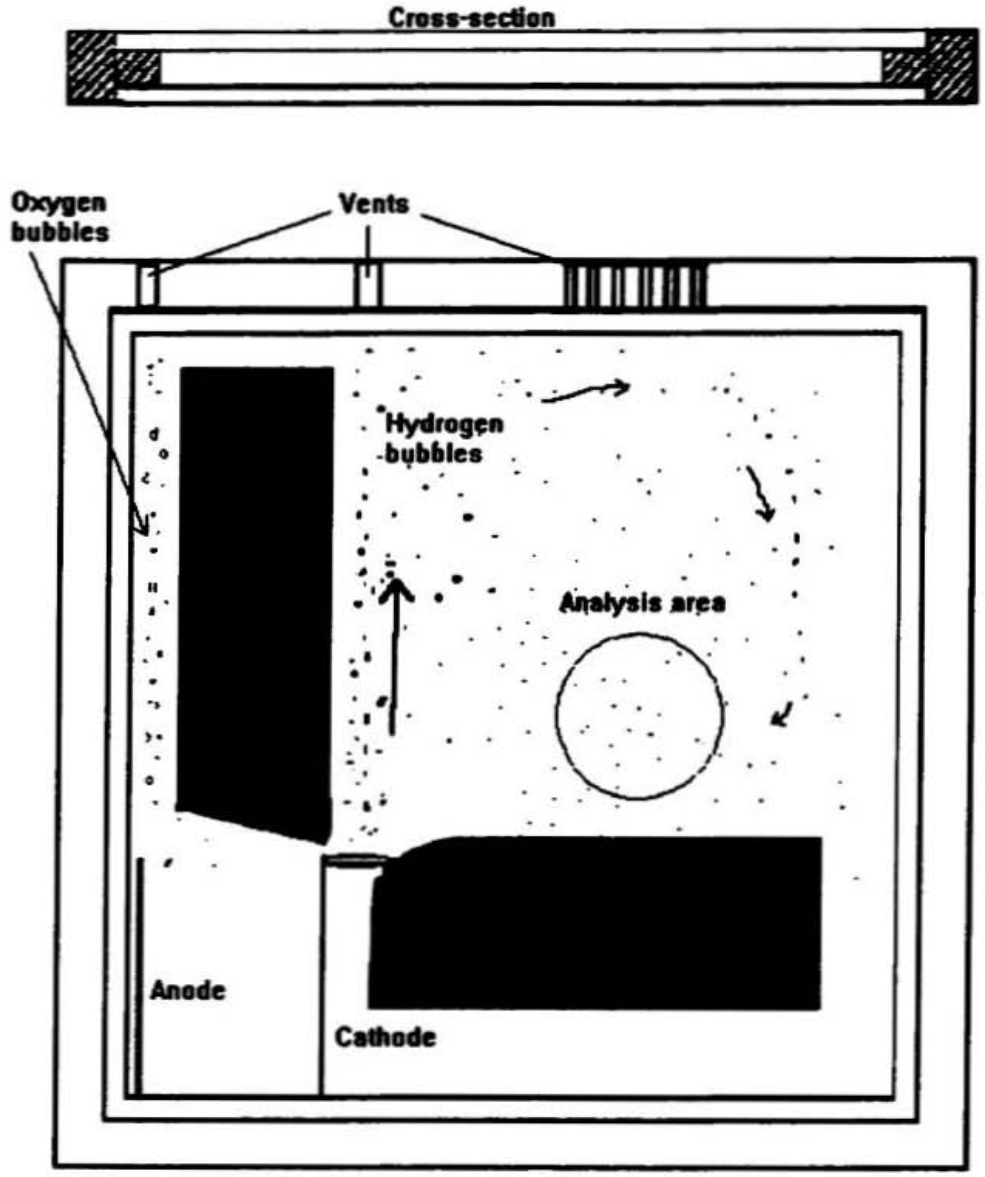

Figure: 4.1

Schematic of the cell used. The cell generated bubbles of the desired size and size distribution within the analysis area shown.

creating an internal current that trapped the smaller bubbles and circulated them around the cell. Near the analysis area the small bubbles have almost zero mean velocity since the downward flow of the current essentially balances the opposing Stokes' velocity, creating a slowly moving random motion between the bubbles.

The geometry and arrangement of the electrodes was also an issue. A number of different cathode shapes were evaluated in an effort to achieve a narrow bubble size distribution, but our measurements did not show a large difference in size distribution for different electrode geometries. For simplicity of construction and cleaning, we used a simple cathode made from 0.25 mm platinum wire wound into a horizontal loop about 15mm in length and 3mm in width. The anode was made of a 7 cm length of the same platinum wire, positioned vertically. Due to blackening that developed over long periods of time, the electrodes had to be periodically cleaned. This was done by rubbing the electrode with a very fine emory cloth then soaking it in a solution of 10% Nitric acid for 20 minutes. The electrodes were then rinsed in nano-pure reverse osmosis water for 30 minutes.

The cell was filled with a solution of 1% Na_2SO_4 and 1% sodium dodecyl sulfate (SDS), by weight, in nano-pure reverse osmosis water. Extreme care was taken with regards to cleanliness and the purity of every material used in the cell. Despite this, we found that our electrodes (mainly the cathode) would blacken. The true source(s) of the blackening was not identified but it is believed to be due to stray metal ions from solder joints depositing on the electrodes. The solder joints were later moved outside of the cell, isolated from the solution. After this modification, thorough cleaning, and

improvements in the purity of the materials used, the blackening was kept to a minimum.

4.3 Bubble Sample Area

The bubble size distribution varied over rather small length scales in the area of the cell sampled by the ultrasonic pulse (~1cm). Therefore reproducibility in the positioning of the receiving transducer was very important. To insure reproducibility we carefully marked the position of the transducer on the cell wall and realigned it to this position before each experimental run. We wanted the bubbles in the sample area to have random motion and no large temporal fluctuations in concentration or size distribution. The area chosen for analysis was initially determined empirically through visual inspection, by looking for an area where the bubbles had small, random motion. We refined the choice of the analysis area by looking at our ultrasonic data. We chose an area that gave reproducible results by averaging and comparing many ultrasonic pulses. For every concentration used the analysis area was videotaped for several minutes using a video microscope. Independent frames where then captured from the VCR with a frame grabber card. These individual frames where then analyzed using commercial imaging analysis software [15] to determine the bubble size distribution and concentration.

4.4 Results

4.4.1 Bubble Size distribution

Bubble sizes were determined from the video data. A frame containing a reference object of a known size was recorded. We could then measure the size of any object in other frames. Each frame was digitally smoothed and thresholded, so that bubbles appeared black and background, white. The threshold intensity was an important parameter since it directly affected the mean bubble size. Using the image analysis software we then determined the lengths of the major and minor axes of each bubble. Since the major axis could be anomalously large if two bubbles were superimposed in the image, we only considered the minor axis. These values were then binned and the data displayed in histograms. We then fit functions to these distributions for use in the theoretical calculations. Fig. 4.2 shows histograms of the bubble size distribution for different electrical currents. Also displayed on the graphs are polynomial fits, which were used in the calculation of attenuation, phase and group velocity, using the theory described in Chap. 2. The coefficients for the polynomial fits are given in Table 4.1. However, as described in Chap. 5, when the polynomial functions were used in the theoretical model, the fits to the experimental data were quite poor. This suggests that the size distributions found through imaging techniques may have been inaccurate due to dust or other impurities. Particles that were not bubbles would have affected the ultrasonic pulses much differently. For a better fit of the theory to our data we used a

Gaussian distribution for the bubble sizes with the mean and standard deviation chosen to give a good fit. This is discussed in Chap. 5.

For the ballistic measurements we used a thin sample cell (4.5 mm) and relatively small currents of 10, 15, 20 and 25 mA. These currents produced the lower concentration of bubbles that was necessary for the ballistic analysis. Surprisingly, the mean bubble size stayed relatively constant at the different currents used. Our mean bubble size was in agreement with other experimental findings (average bubble radius, 11-18 μm) using the same method of bubble generation [16].

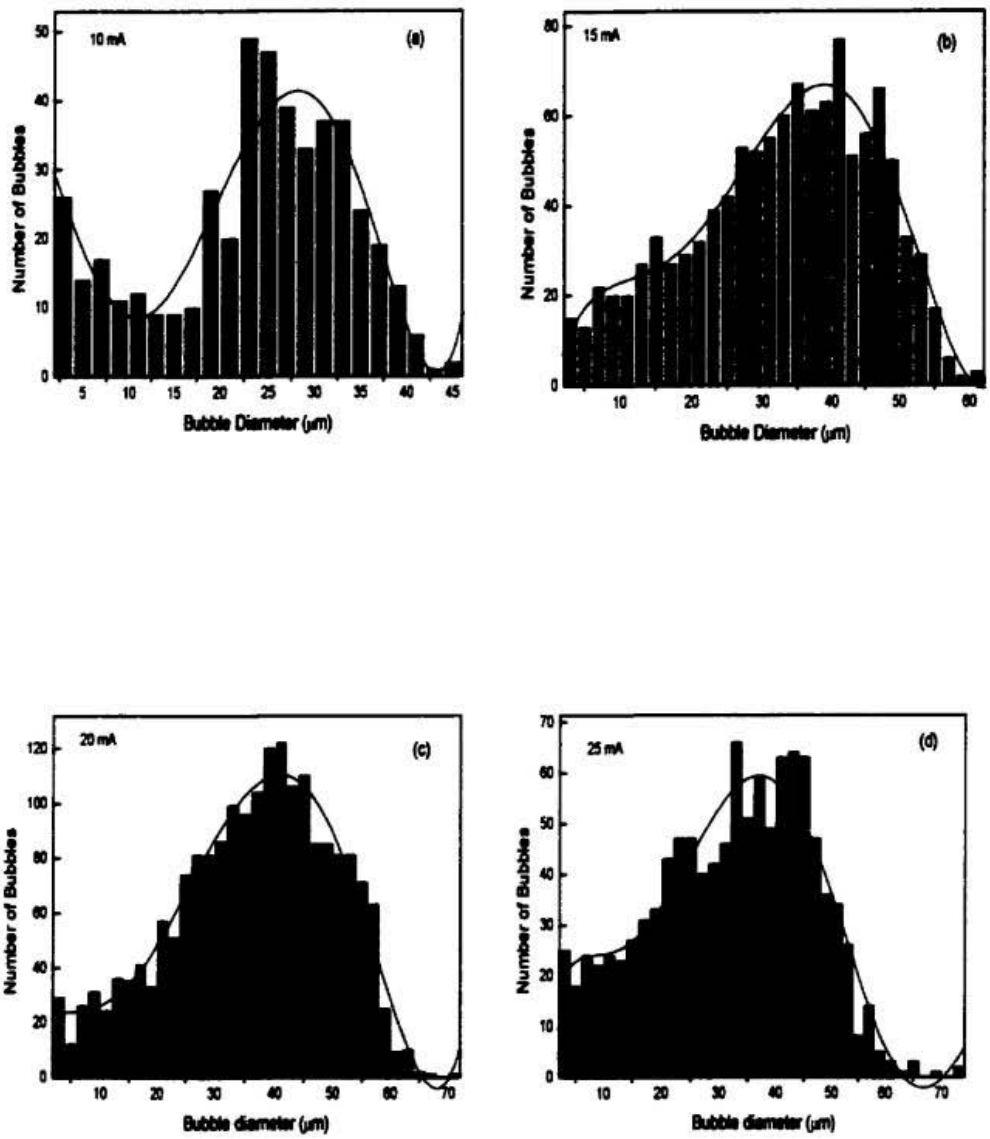

Figure: 4.2

Histograms showing the number of bubbles as a function of size.

Histograms are shown for currents of (a) 10mA, (b) 15mA, (c) 20mA, and (d) 25mA.

The lines are polynomial fits to the bubble size data.

Current (mA)	Polynomial fit to bubble size distribution $f(r)=b_0+b_1(2r)+b_2(2r)^2+b_3(2r)^3+b_4(2r)^4+b_5(2r)^5+b_6(2r)^6$						
	b0	b1	b2	b3	b4	b5	b6
10	64.38	-3.321	-0.2292	0.04124	-1.42E-03	1.44E-05	0
15	-2.949	6.689	-0.677	0.0326	-6.36E-04	4.17E-06	0
20	21.18	1.127	-0.2086	0.0183	-4.31E-04	3.09E-06	-1.68E-09
25	11.67	4.47	-0.6096	0.0378	-9.98E-04	1.15E-05	-4.76E-08

Table: 4.1

The coefficients of a polynomial fit to the histograms in Fig. 4.2.

4.4.2 Bubble Concentrations

In order to calculate the bubble concentration, or void fraction, of the sample medium we used a different image analysis technique. Images were taken at a larger field of view (~10 mm^2, about 3mm across). The large field of view allows for better statistics, and also to brings into focus all the bubbles within the sample thickness. The images were again smoothed and thresholded. Then the projected area of all the bubbles in the image was summed. We refer to the total area of all the bubbles within the image as A_{tot}. We can solve for the number of bubbles N_b by dividing the total area of the bubbles by the area of a single average bubble area, A_{bub}. We have

$$N_b = \frac{A_{tot}}{A_{bub}}. \tag{4.1}$$

To find the total void fraction, ϕ we multiply the number of bubbles by the volume of one average bubble, V_{bub}, then divide by the total volume in the image, V_f.

$$\phi = \frac{N_b V_{bub}}{V_f} \tag{4.2}$$

The calculated void fractions are recorded in Table 4.2. Using this robust calculation, we found values that were on the same order of magnitude as the values used to compare the theory to data in Sec. 5.5.

Current	Average radius from images	Void fraction from images
(mA)	(microns)	(parts per million)
10	11.85	3.7
15	16.5	23.4
20	18.1	26.8
25	16.1	31.6
30	not calculated	59.7
40	not calculated	86.1
50	not calculated	119.8

Table: 4.2

A tabulated comparison of the void fractions and average radius found in the image analysis.

5 Results

5.1 Introduction

In this chapter, the experimental results are presented and compared to theoretical predictions. We first describe how the measurements were performed. We then present quantitative measurements of the attenuation for different bubble concentrations and compare the data to theoretical calculations (Sec. 5.3). The attenuation is closely related to the extinction length, as described in Sec. 5.3.1. We also measured the phase and group velocities for different concentrations. The methods used to determine the phase and group velocities are discussed in Sec. 5.4.1 and 5.4.2 respectively. The data are then presented and compared to the theoretical expectations.

5.2 Ballistic measurements

In a medium with strong scattering, the total transmitted signal is composed of two components. The component in which we are interested is the ballistic component, which propagates coherently straight through the sample without scattering away from the incident direction. In addition, there is an incoherent scattered component that varies in both amplitude and phase across the output face of the sample. The characteristics of waves propagating ballistically through the sample were determined by comparing the coherent component of a pulse that travels through the sample with a reference pulse. These contributions either travel through the medium without scattering or are scattered in the forward direction, and are coherent with the original pulse [18, 19]. The scattered component is made up of waves that have traveled a large number of possible paths through the sample. As the sample thickness, or the concentration of the bubbles within the sample increases, the number of scattering/absorption sites and so the number of possible paths for a pulse to take increases. The wave pulses' incoherent portion then becomes more prominent, and the coherent portion less obvious. As the pulse scatters from one of the bubbles, the spectrum of both its frequencies and wave vectors can be affected. In addition, the scattering can cause the pulse to arrive later in time due to its taking a longer path. The energy can also be absorbed and then released later in time. These combined effects changing the temporal and spatial phase properties of the scattered pulse, and when the scatterers are moving cause the scattered sample pulse to vary a great deal from one pulse to the next. Thus, we find the coherent component of

the pulse by averaging many pulses together. An example is shown in Fig. 5.1. The pulses shown in the figure are 1 MHz pulses with an incident pulse width of 7 μs that have traveled through the sample. At this frequency, the effects of scattering are quite pronounced. Fig. 5.1 (a) displays three consecutive pulses taken 0.5 seconds apart. Fig. (b) shows an average over 10,000 pulses under the same conditions. The signal at longer times, which is due to that portion of the pulse which is multiply scattered and so takes a longer time to reach the detector disappears on averaging, leaving the coherent ballistic signal. This coherent ballistic pulse can now be compared to the reference pulse to obtain data for the attenuation, the group velocity and the phase velocity. The specific techniques used to extract these data are explained in the sections to follow.

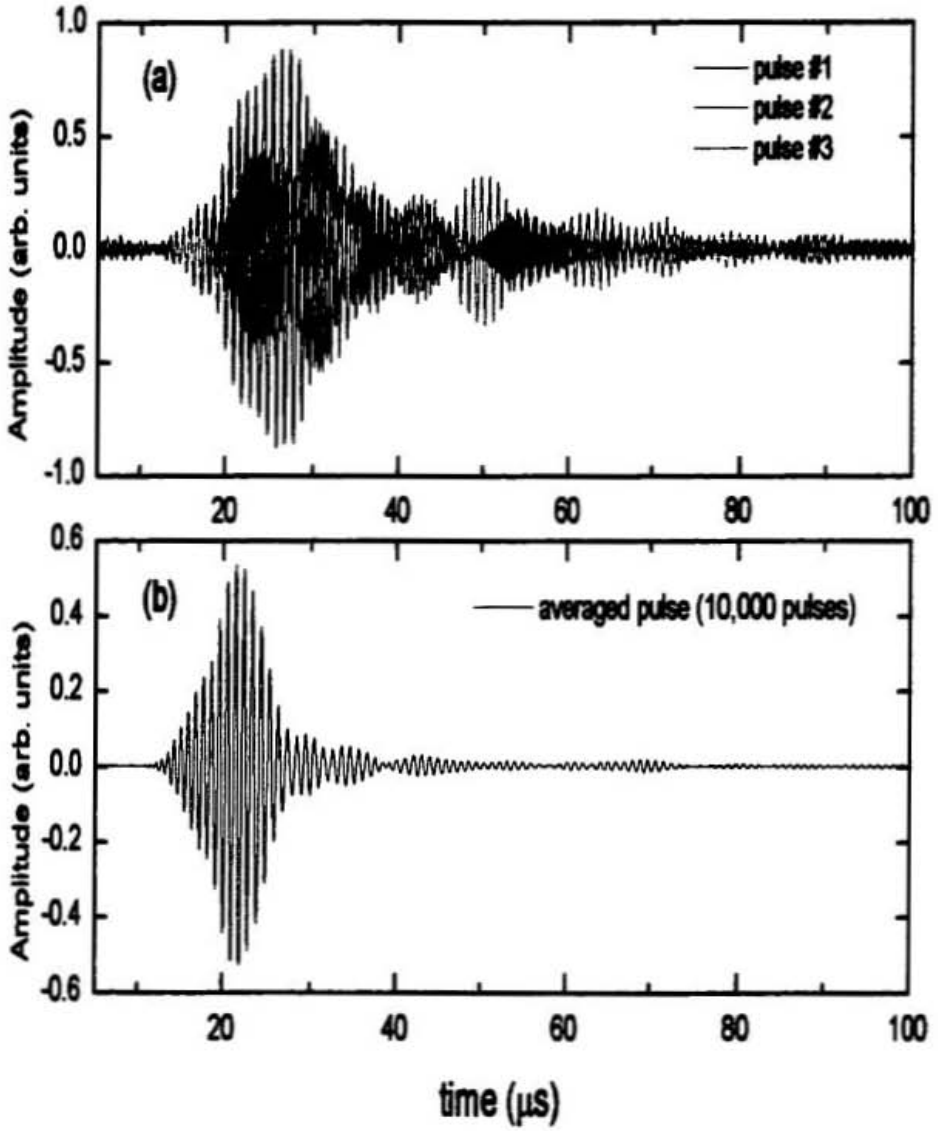

Figure: 5.1

The coherent pulse (b) was found by averaging 10 000 individual pulses (a) under the same experimental conditions.

5.3 Attenuation

The attenuation coefficient describes the decay of a wave with distance traveled. A wave with intensity I_0 at position z_0 decays to

$$I(z) = I_0 e^{-\alpha(z-z_0)}$$

at position z, where α is the attenuation coefficient and, at a given frequency, is a characteristic of the medium. Setting the distance traveled equal to the cell thickness L, we have

$$I = I_0 e^{-\alpha L}, \tag{5.1}$$

where I is the intensity of the wave leaving the cell.

We measure the attenuation coefficient by taking ratio of the FFT (fast Fourier transform) of the sample pulse to that of the reference pulse. The reference pulse is recorded with the cell in place but without any bubbles in the liquid. We take the intensity of the reference pulse, I_{ref}, as I_0. What is measured is the pressure due to the sound pulse, so the amplitude of the FFT is proportional to the pressure. Since the sound intensity is proportional to the square of the pressure, we have

$$\frac{I_{sam}}{I_{ref}} = e^{-\alpha L} = \left(\frac{P_{sam}}{P_{ref}}\right)^2 = \left(\frac{FFT_{sam}}{FFT_{ref}}\right)^2. \tag{5.2}$$

Here P_{sam} and P_{ref} are the measured sample and reference pressures respectively.

In our measurements attenuators were used to avoid high power signals that would saturate the inputs of the experimental equipment, so the measured FFT amplitudes must be corrected for this. The equation

$$db = 10\log\left(\frac{I}{I_0}\right) = 20\log\left(\frac{P}{P_0}\right) \tag{5.3}$$

gives the ratio of the intensities in dimensionless units known as decibels. These are the same units used by the attenuators. The unattenuated pressure signal, P_{db_0} is the sum of our measured signal in decibels, P_{db} plus the amount of attenuation a_{db} inserted by the attenuators. Therefore,

$$P_{db_0} = P_{db} + a_{db}. \tag{5.4}$$

The difference between the reference and the sample pressure signals (in db) is then be

$$P_{db_0}^{ref} - P_{db_0}^{sam} = P_{db}^{ref} - P_{db}^{sam} + \left(a_{db}^{ref} - a_{db}^{sam}\right), \tag{5.5}$$

where the subscript *0* defines unattenuated values. Using Eq. (5.3), we can write Eq.(5.5) as

$$P_{db_0}^{ref} - P_{db_0}^{sam} = 20\log\left(\frac{P_0^{ref}}{P_0^{sam}}\right) = 20\log\left(\frac{P^{ref}}{P^{sam}}\right) + \left(a_{db}^{ref} - a_{db}^{sam}\right). \tag{5.6}$$

Rearranging Eq. (5.6) we have

$$\frac{P_0^{sam}}{P_0^{ref}} = \frac{P^{sam}}{P_0^{ref}} 10^{\frac{-(a_{db}^{ref} - a_{db}^{sam})}{20}}. \tag{5.7}$$

We identify the attenuation correction factor as

$$corr = 10^{\frac{-(\alpha_{@}^{ref} - \alpha_{@}^{sam})}{20}}. \tag{5.8}$$

Inserting this factor into Eq. (5.2) we have

$$\frac{I_0^{sam}}{I_0^{ref}} = e^{-\alpha L} = \left(\frac{P^{sam}}{P^{ref}} 10^{\frac{-(\alpha_{@}^{ref} - \alpha_{@}^{sam})}{20}} \right)^2 = \left(\frac{FFT_{sample}}{FFT_{reference}} 10^{\frac{-(\alpha_{@}^{ref} - \alpha_{@}^{sam})}{20}} \right)^2, \tag{5.9}$$

corrected for the attenuators used. We can now solve for the attenuation coefficient,

$$\alpha = -\ln\left(\frac{FFT_{sam} corr}{FFT_{ref}} \right) \frac{2}{L}. \tag{5.10}$$

Fig. 5.2 shows the measured attenuation coefficient at various bubble concentrations corresponding to currents from 10 to 25 mA. The most obvious feature is that at the resonance frequency the attenuation is at a maximum. The attenuation is made up of contributions from both scattering and absorption. These contributions can be separated using the acoustic cross-sections that were introduced in Chap.2. We can write α in terms of the absorption and scattering cross sections as

$$\alpha = n_b(\sigma_s + \sigma_a), \tag{5.11}$$

where n_b is the number density, being the total number of bubbles in a cubic meter. σ_a is the absorption cross-section and σ_s the scattering cross-section. Values of σ_a and σ_s

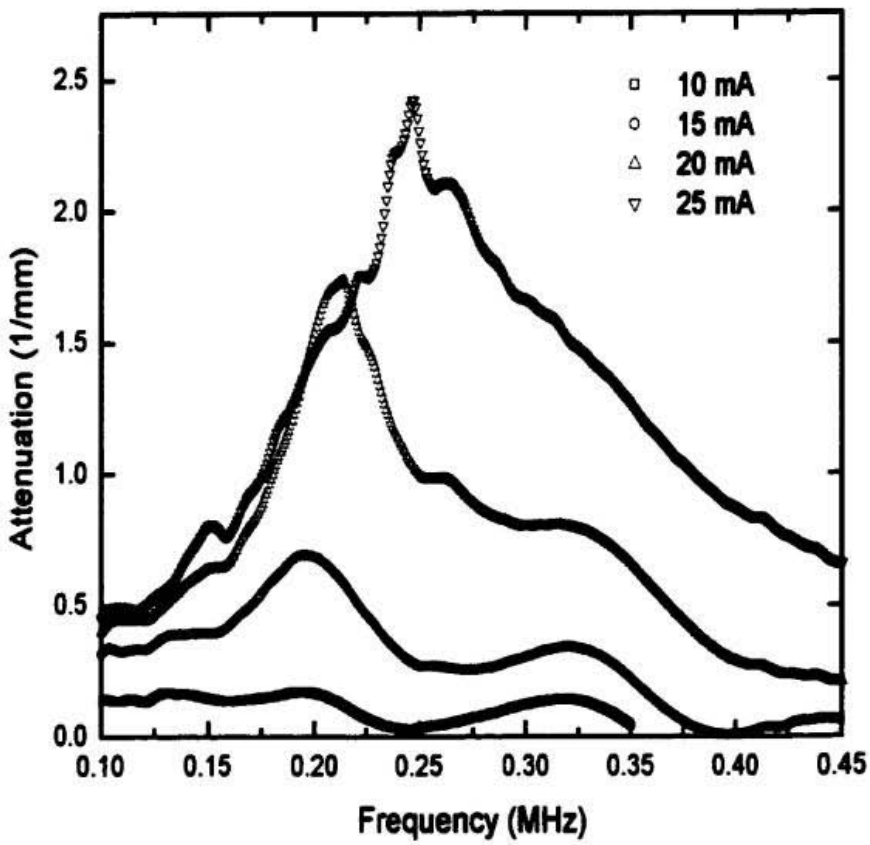

Figure: 5.2

The attenuation coefficient as a function of frequency at various concentrations.

calculated from Eqs. (2.27 and 2.28) are shown in Fig. 2.2. Although both the scattering and absorption are at a maximum at resonance, we can see that the absorption dwarfs the scattering cross-section there. The importance of this feature of our medium will be clear later in this chapter.

The attenuation data in Fig. 5.2 show a second, weaker peak at about 0.33 MHz, especially at small currents (low bubble concentrations). We believe this is due to multiple reflections between the two cell walls at resonance. These reflections are most prominent in the reference pulses, which were taken with the cell in place and with a bubble free liquid, since when bubbles are present the bubble solution quickly attenuates any reflections. If we use the equation for the wavelength λ_n of a standing wave,

$$\lambda_n = \frac{2L}{n}, \tag{5.12}$$

where $n = 1, 2, 3\ldots$ When we substitute the cell thickness, L=4.5mm, the first few standing wave lengths are

$$\lambda_1 = 9\text{mm},$$
$$\lambda_2 = 4.5\text{mm},$$

and

$$\lambda_3 = 3\text{mm}.$$

Knowing the wave speed in a bubble free liquid is 1500 m/s, we can determine the corresponding resonant frequency harmonics to be;

$$f_1 = 0.167\text{MHz},$$
$$f_2 = 0.33\text{MHz},$$

and

$$f_3 = 0.5\text{MHz}.$$

Because these harmonics are present in our reference data, their effects can be seen in the ballistic data at the corresponding frequencies. The first harmonic, although visible, is not as pronounced as the second at 0.33 MHz. This could be due to the effects of the first

harmonic frequency being overwhelmed by the bubble resonance. The small effects of the higher harmonics are simply due to the weakness of the signal after multiple reflections.

5.3.1 Extinction Length

The extinction length l_{ext} is a measure of the distance traveled by the wave before it is scattered or absorbed. It is simply the inverse of the attenuation coefficient,

$$l_{ext} = \frac{1}{\alpha}. \tag{5.13}$$

Substituting this into Eq. (5.1) we have,

$$I = I_0 e^{-\frac{L}{l_{ext}}}. \tag{5.14}$$

where L is the thickness of the sample. l_{ext} is the distance over which the intensity of the incident pulse decays by a factor of e^{-1}, due to a combination of absorption and scattering. If l_a is the absorption length and l_s is the scattering length, then l_{ext} is given by,

$$\frac{1}{l_{ext}} = \frac{1}{l_s} + \frac{1}{l_a}. \tag{5.15}$$

This measurement gives us a better understanding of the spatial properties of the medium. Near resonance the attenuation is nearly entirely absorptive, therefore the extinction

length, near resonance is approximately equal to l_a. l_{ext} is shown as a function of frequency for concentrations of 15, 20, and 25 mA in Fig. 5.3.

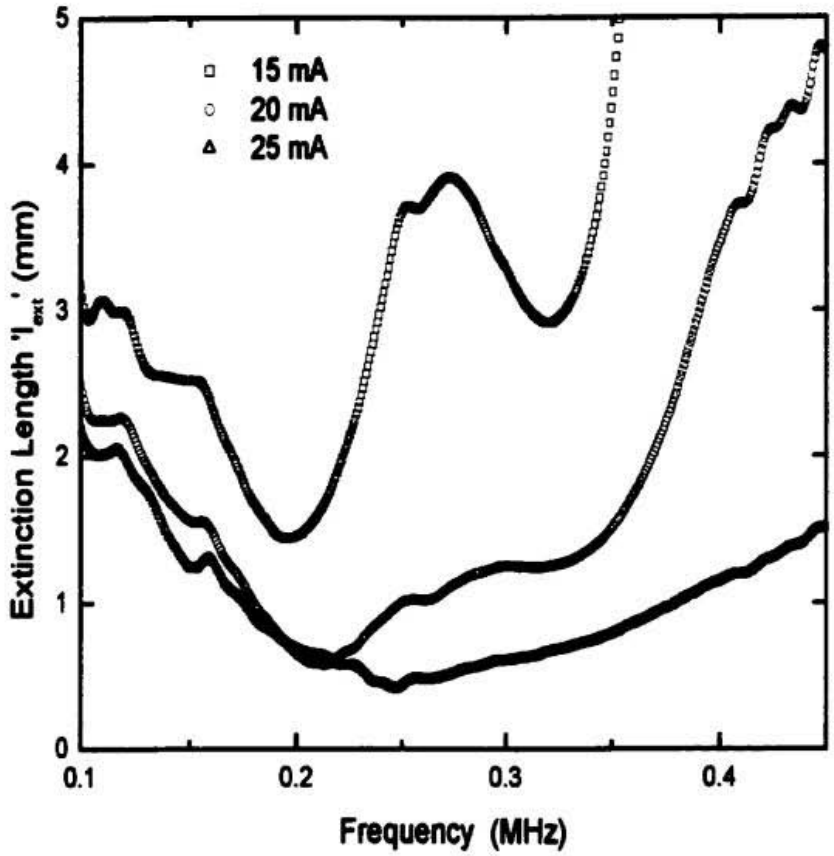

Figure: 5.3

The extinction length as a function of frequency at various bubble concentrations.

Figure 5.3 shows data for the higher concentrations of 15, 20, and 25 mA with the shortest extinction lengths. The lower concentration of 10 mA had a larger minimum extinction length than the thickness of the cell so the data was not shown. In every case,

the extinction length is smallest at resonance, where inversely the attenuation is the greatest. For the 15 mA data we can see another dip in l_{ext} at approximately 0.33 MHz, due to the multiple reflections mentioned above. This observation further confirms that this is an effect of standing waves between the two walls, where the bubbly liquid is contained, since at higher concentrations these reflections are attenuated and damped out.

5.4 Phase and Group Velocities

The phase and group velocities were measured using the same data as was used for the attenuation measurements. In the velocity measurements we are not concerned with the amplitudes of the wave pulses so the attenuation correction discussed above was not needed. We did have to worry about the time relation between the reference (bubble free liquid) and sample (bubbly liquid) pulses. In order to calculate the time it takes for the carrier wave (phase velocity) or packet (group velocity) to traverse the sample we had to correct the timing by 'zeroing' the reference time. This is done by subtracting the time it takes for the pulse to travel through the medium without bubbles. Fig. 5.4 shows the path traveled by the reference and sample pulses. The generating and receiving transducers are at a fixed distance from each other. The time taken for the reference pulse to travel across the cell is

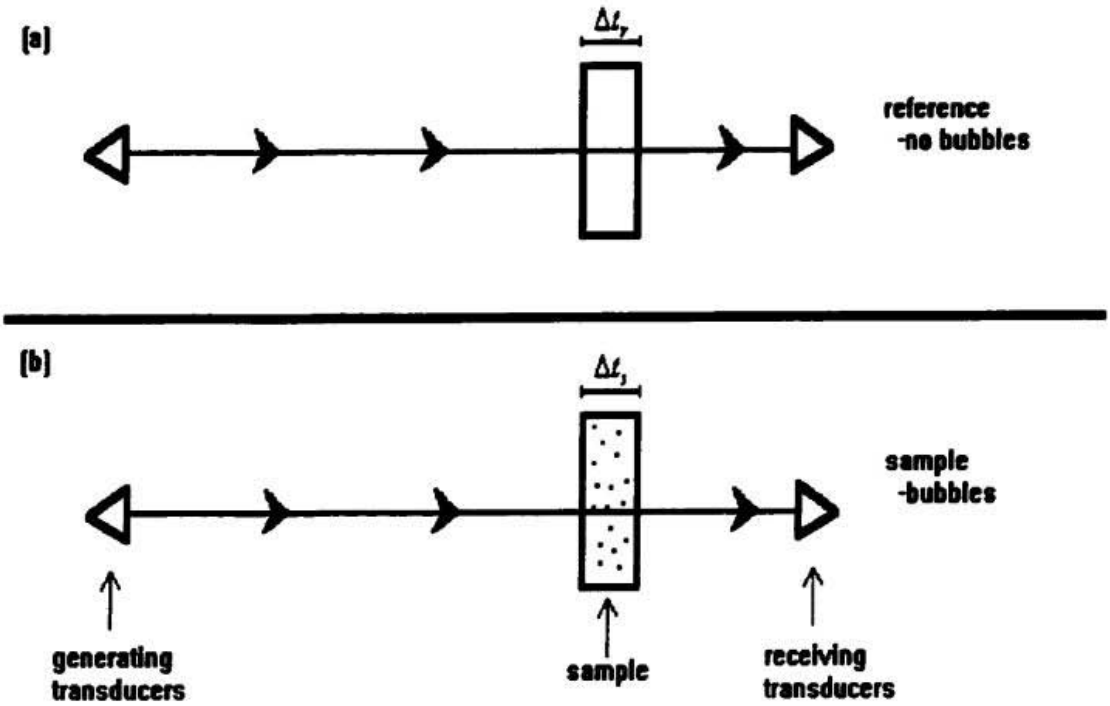

Figure: 5.4

The reference and sample pulse travel paths. In the reference (a) the pulse travels through a medium containing a bubble free liquid. In the sample measurements (b) the medium contains bubbles.

$$\Delta t_r = \frac{L}{v_{water}},$$

where L is the thickness of the cell and v_{water} is the speed of sound in water. If we subtract the time scale of the reference data by this amount, we are effectively removing the cell from the path of the reference pulse. Since the cell walls are common to both the reference and sample pulses, they were not considered in the time correction. Once this time correction has been applied, the difference in time between the reference and sample data Δt_s is the time it takes for the pulse to travel through the bubbly medium.

5.4.1 Phase Velocity

The phase velocity is the speed of the sinusoidal carrier wave. We can find the phase velocity by measuring the propagation speed of a particular crest, for example. The distance that the crest propagates, for a sample of thickness L, divided by the time to do so, t_{wave}, gives us the simple equation

$$V_p = \frac{L}{t_{wave}}. \tag{5.16}$$

We actually determined the phase velocity by measuring the phase difference between the Fourier components of the reference and sample pulses. The phase difference $\Delta\phi$ is directly related to the wave propagation time within the medium at a given frequency,

$$\Delta\phi = \omega t_{wave}. \tag{5.17}$$

Here ω is the angular frequency of the Fourier component. Substituting Eq. (5.17) into Eq. (5.16) we have

$$V_p = \frac{\omega L}{\Delta\phi} = \frac{2\pi fL}{\left|\phi_{ref} - \phi_{sam}\right|}, \tag{5.18}$$

where f is frequency. The FFT phase angles for typical reference and sample data are plotted in Fig.5.5.

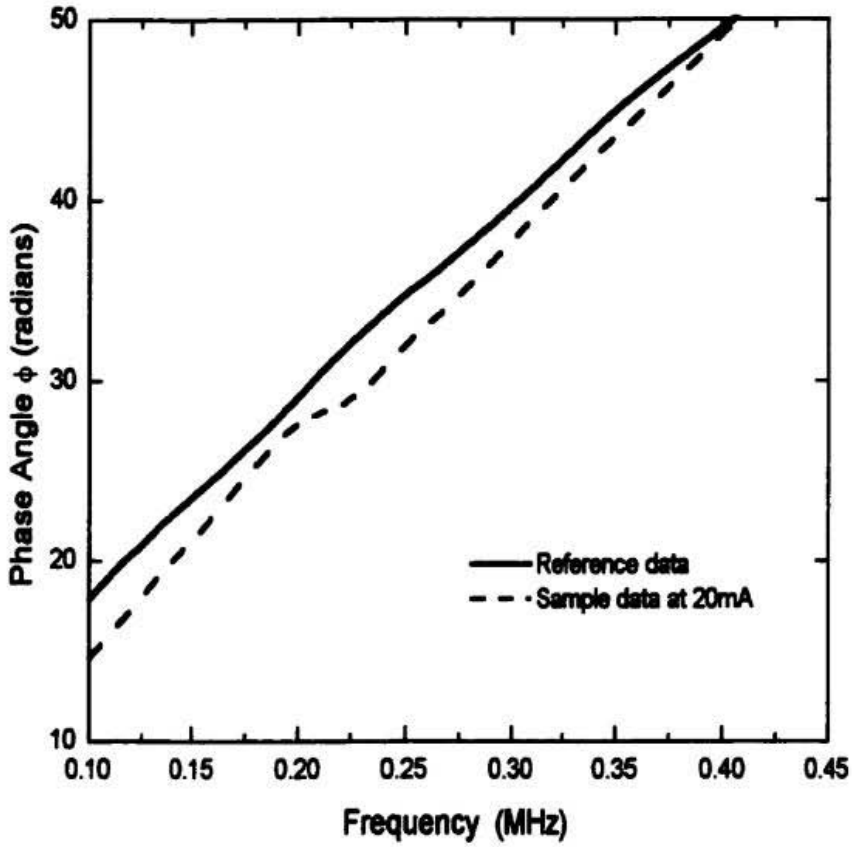

Figure: 5.5

Typical plot of the measured phase angle of both reference and sample data.

Often Eq. (5.18) is incomplete, as the phase difference can only by determined to within $\pm 2\pi n$, where n is an integer. We compared the oscillations with the greatest amplitude (having the best definition) to get a rough idea as to the value of the phase velocity. We will call this value V_{Pest}. We then compare adjacent crests that have a difference of one period in time with the original phase velocity value. We verified our

measurements by finding the phase velocity at a high frequency (>1MHz). The phase velocity through the medium at high frequencies has very little dispersion, and it is near the velocity in the bubble free liquid. We then follow the phase velocity for lower frequencies, and keep it consistent with high frequency measurements by adding or subtracting an integer number of periods. Dropping the *wave* subscript, the corrected time for the wave travel time is,

$$t_{new} = t_{old} \pm nT, \tag{5.19}$$

where $T = 1/f$ is the period of the travelling wave, and $t_{old} = L/V_{P_{old}}$ is the uncorrected propagation time. Substituting this into Eq. (5.16), we arrive at

$$V_p = \frac{V_{P_{old}}}{1 \pm {}^{nV_{P_{old}}}/_{Lf}}. \tag{5.20}$$

We can see the effects of adding and subtracting periods in Fig. 5.6, where we have plotted the 20 mA phase velocity data along with velocities obtained by adding and subtracting one or two periods.

A plot of the phase velocity data for currents ranging from 10 mA to 20 mA is shown in Fig. 5.7.

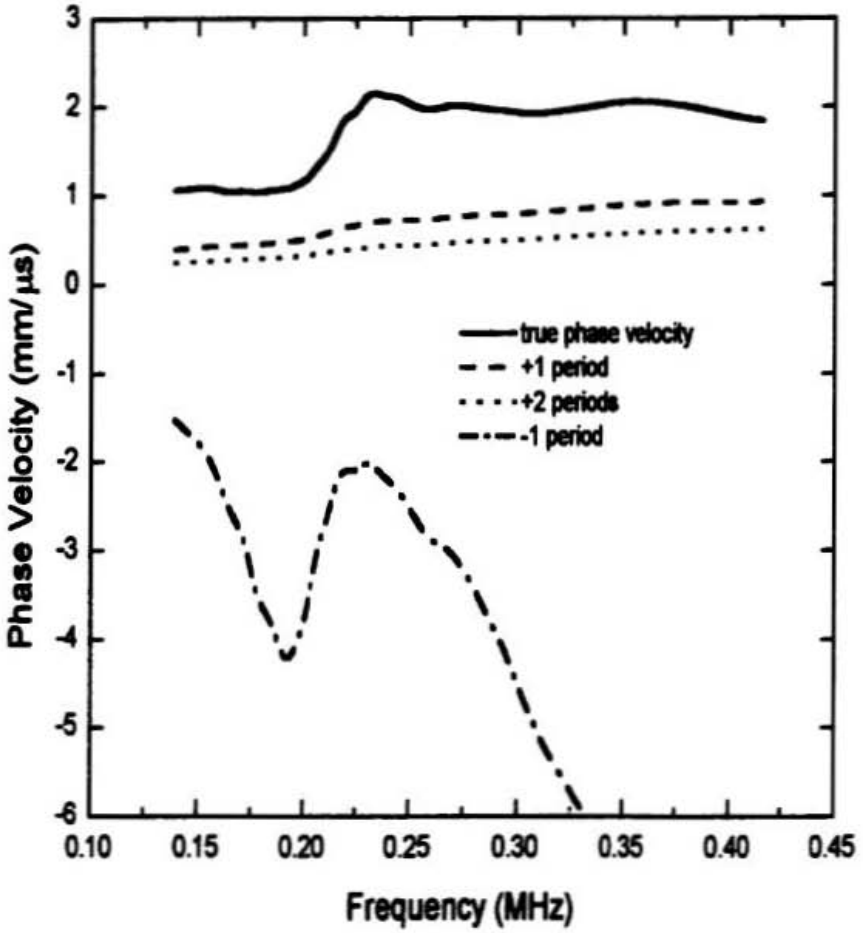

Figure: 5.6

The phase velocity for the 20 mA sample compared with the velocity calculated using period shifts of n= +1, +2, and -1.

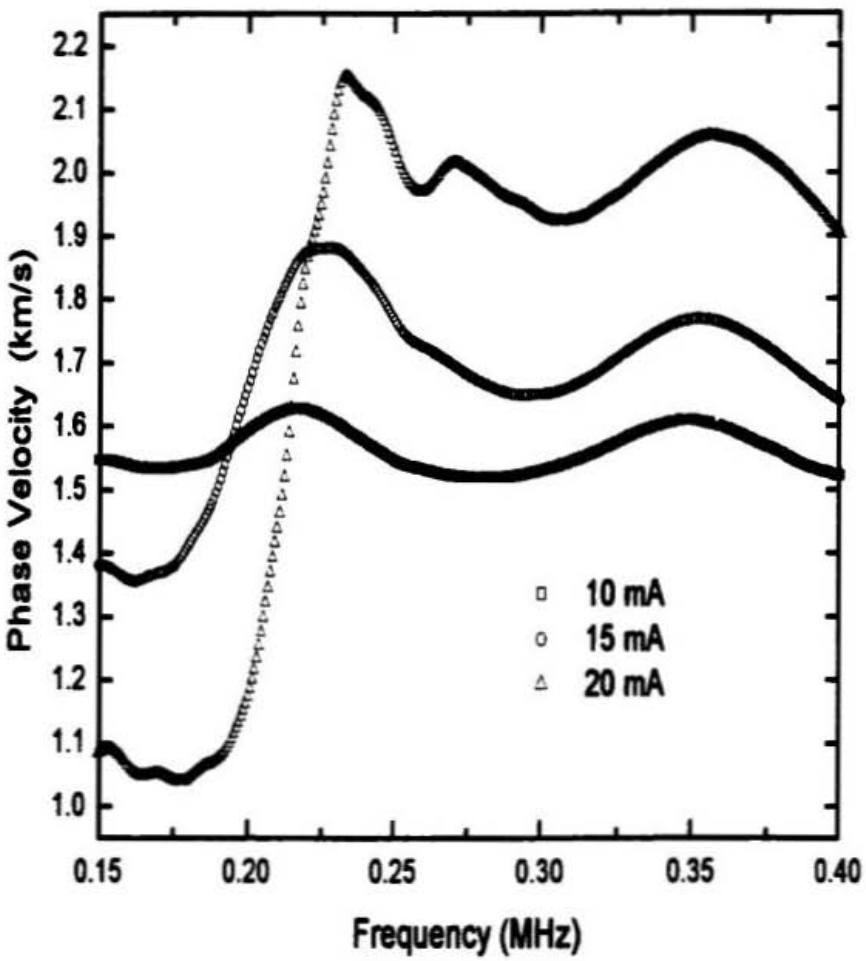

Figure: 5.7

The phase velocity as a function of frequency near resonance.

The resonant frequency is about 0.2 MHz.

In a non-dispersive medium, the phase velocity is equal to the group velocity and does not change with frequency. In Fig. 5.7, we can see how the phase velocity changes due to the dispersion of our medium. The phase velocity is a function of frequency. The bubble-free solution has a phase velocity of about 1500 m/s. If we look at the 20 mA data, we see that V_p is less than that in the bubble free solution below the resonant frequency f_0 ($f_0 \approx 0.2$ MHz). V_p increases as f approaches f_0. At frequencies just above the resonance, we can see the wave speed is higher than that in the bubble free liquid. As we go higher in frequency, and further above the resonance, the phase speed decreases again towards 1500 m/s. This is due to the medium being less dispersive away from resonance. As the concentration becomes greater, this effect on the phase velocity around resonance is more pronounced.

A second increase in phase velocity can be seen at about 0.35 MHz. We believe this is due to multiple reflections between the two cell walls as discussed in Sect. 5.3.

5.4.2 Group Velocity

The group velocity V_g was measured in a very different way. V_g is the speed of the peak of a wave packet. To find V_g, we need to find the time Δt_{packet} it takes for the peak of a wave packet to travel through the sample. The group velocity is then given by

$$V_g = \frac{L}{\Delta t_{packet}}. \tag{5.21}$$

The reference and sample wave pulses were convolved with a Gaussian envelope of a specific bandwidth and center frequency. The convolution was done as a multiplication in Fourier space, followed by an inverse FFT to convert the data back into the time domain. The result is a Gaussian wave packet containing a narrow band of frequencies . By repeating this process for many different center frequencies we divide the original sound pulse into many wave packets, each corresponding to a different Fourier frequency component. In Fig. 5.8 we show an example of this filtering process. The measured reference pulse is shown in Fig. 5.8 (a). The succeeding plots show the pulse after it has been gaussian filtered at a center frequency of (b) 0.3 and (c) 0.4 MHz. In both cases the filter bandwidth was 0.02 MHz. The Gaussian envelope of the filtered wave packet is also shown. The step size between center frequencies was chosen to give adequate frequency resolution in our group velocity measurements. The frequency range in which we could obtain reliable data was taken when both the reference and sample signal intensities were well above the noise level.

In Fig. 5.9, we compare the reference and sample pulses for a typical data set and the envelopes of the filtered wave packets at several frequencies. The bandwidth used for each of the Gaussian filters is 0.02 MHz. Once the envelopes of the wave packets were generated, we fit the peaks to a quadratic using a least squares fit program. We then subtract the time of the peak of the reference envelope, t_{ref}, from the time of the peak of

the sample envelope, t_{env}, giving us the time it takes a pulse at the appropriate frequency to traverse the bubbly medium. We can now evaluate the group velocity using Eq. (5.21).

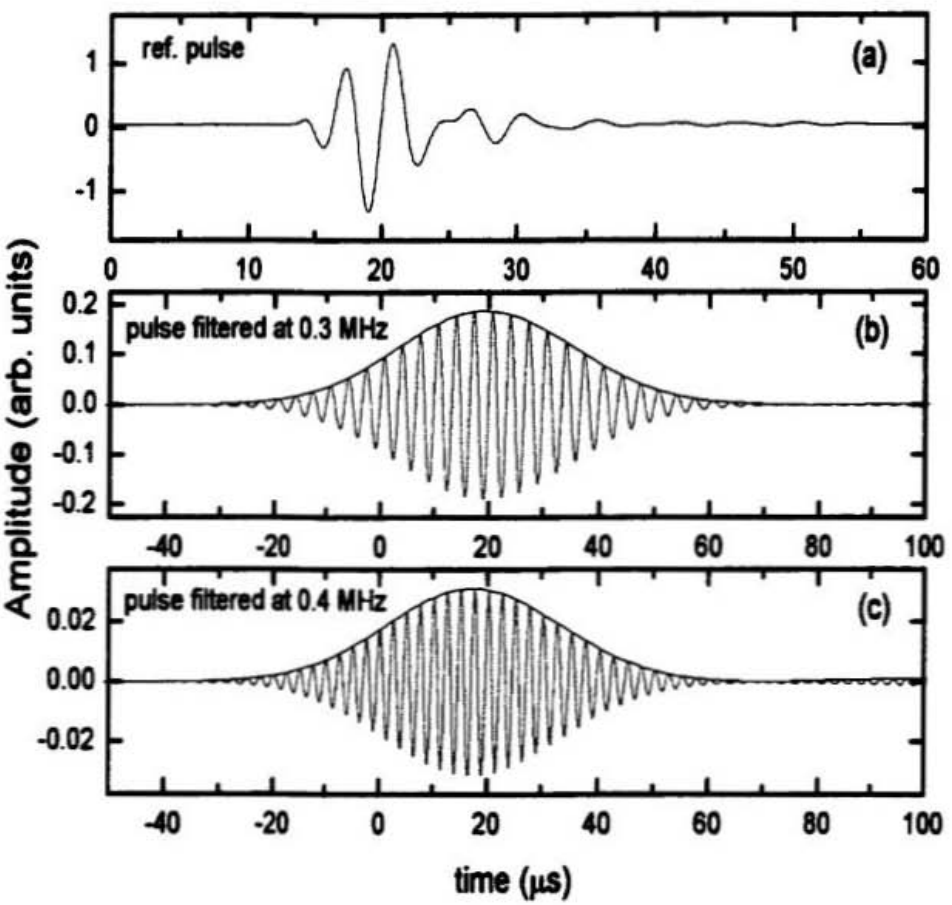

Figure: 5.8

A depiction of the pulse and two filtered wave packets centered at 0.3 and 0.4 MHz respectively. The bandwidth used was 0.02 MHz.

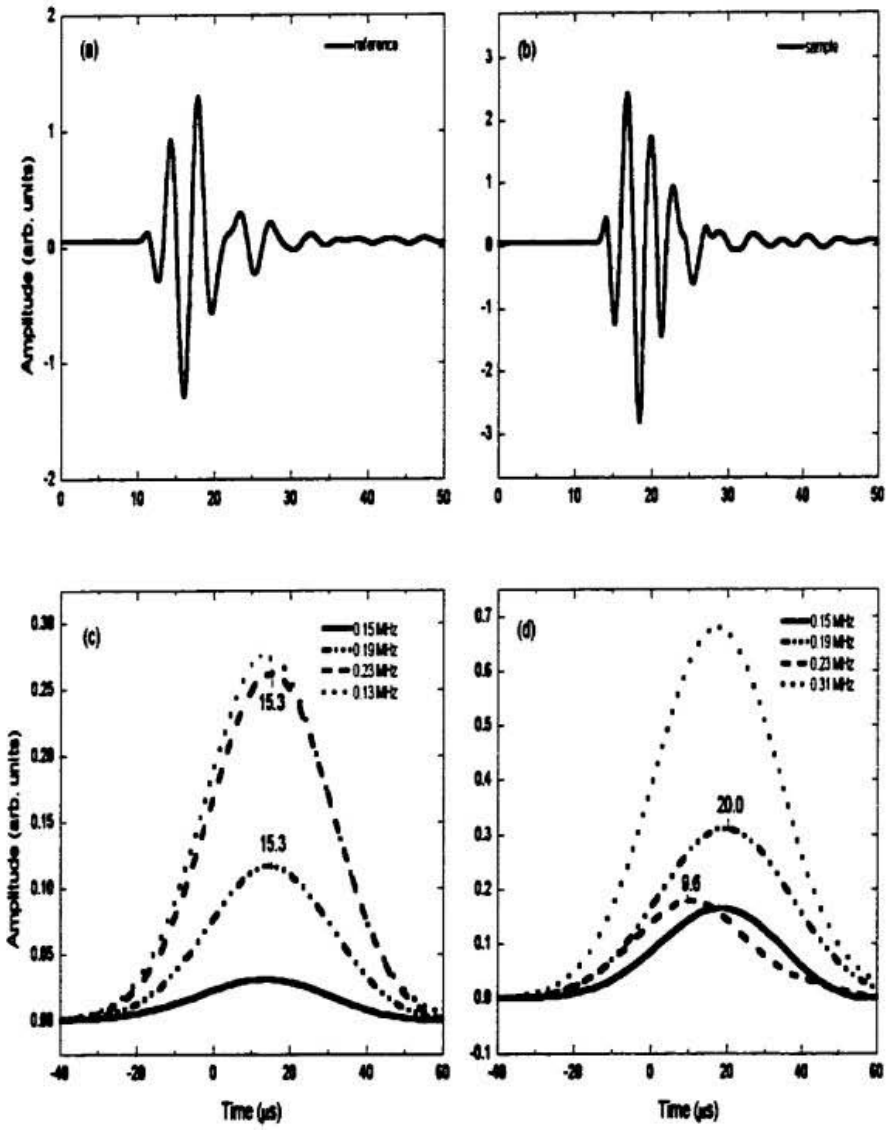

Figure 5.9

Typical reference (a) and sample (b) pulses. (c) and (d) show the Gaussian envelopes of the filtered wave packets at the frequencies indicated. The numbers indicate the time of the peak of the envelope.

We can also see from Fig. 5.9 that the time of the peak of the pulse envelope can change quite substantially with frequency. This is due to dispersion, especially near resonance. If we look at the envelope at 0.23 MHz, we can see that the peak of the sample pulse in Fig. 5.9 (d) occurs at an earlier time than the peak in the corresponding reference pulse, shown in Fig. 5.9 (c). This means at 0.23 MHz, the peak of the pulse has left the cell before the peak of the reference pulse (at the same frequency) has entered the cell. This is a case of negative group velocity. The 0.23 MHz sample pulse is smaller in amplitude than the 0.23 MHz reference pulse, indicating the high absorption that occurs at this frequency. The combination of dispersion and absorption leads to distortion of the total pulse which can be seen by comparing Fig. 5.9 (a) and (b). This is certainly one of the most interesting results of this research. The effect of negative group velocity is shown more clearly in the filtered pulses in Fig. 5.10.

The bandwidth of the Gaussian filter had to be carefully chosen. A very narrow bandwidth corresponds to a wide time pulse and leads to a loss of accuracy in the determination of the peak time. A large bandwidth often leads to a distorted non-Gaussian time pulse, without an easily distinguishable center peak.

The measured group velocities for different concentrations near the resonant frequency are shown in Fig. 5.11. The 10 mA sample is lower in bubble concentration and shows a positive group velocity. While at higher concentrations (15 and 20 mA) the absorption is much higher leading to anomalous dispersion. The group velocity around the bubble resonance becomes negative.

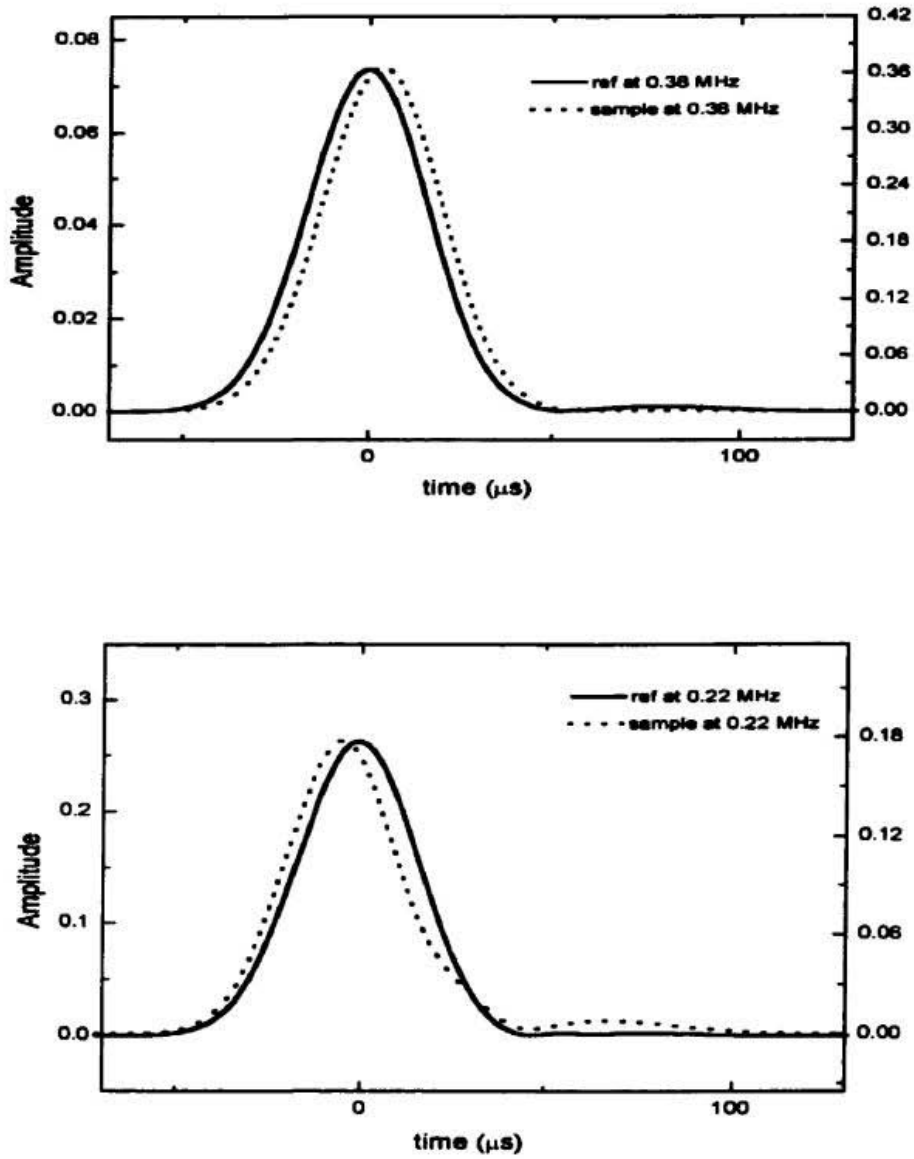

Figure: 5.10

An example of negative group velocity (negative time between the peaks of the wave packets). $t = 0$ is chosen to correspond to the peak of the filtered reference pulse, shown as a solid line. The dotted lines are the sample data from the bubbly medium. The measurement at 0.38 MHz gives a positive group velocity. At 0.22 MHz the peak of the sample pulse is detected before the peak in the reference pulse, producing a negative group velocity.

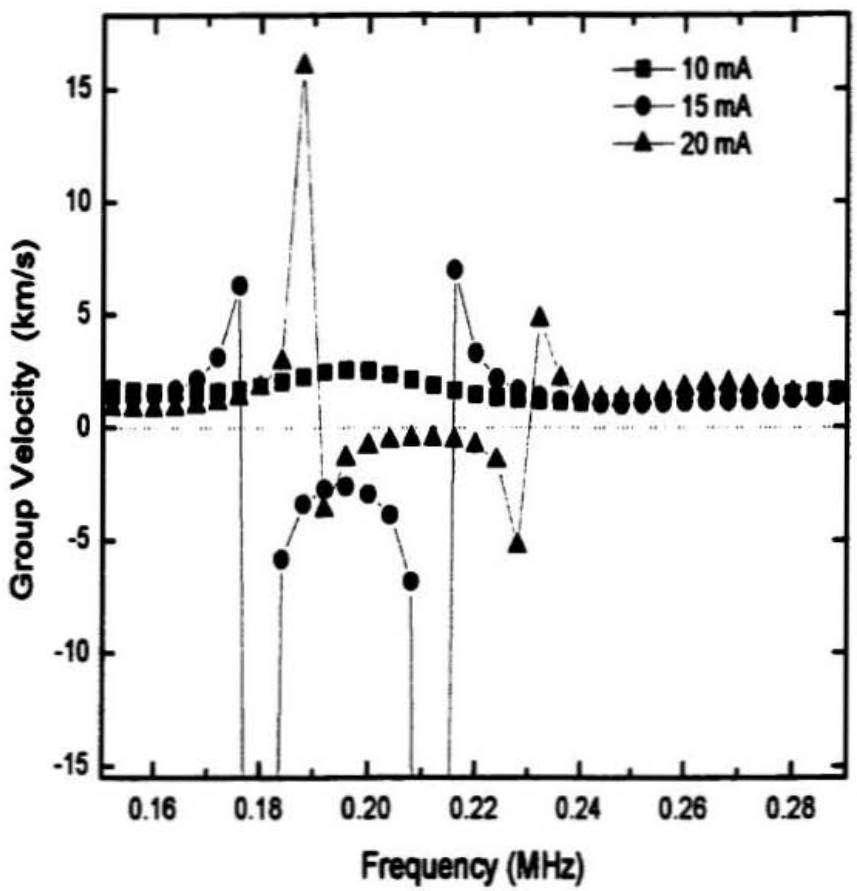

Figure: 5.11

Group velocity as a function of frequency for three different currents near the resonance frequency. The group velocity is negative for currents of 15 and 20 mA.

5.5 Comparison with theory

In this section we compare the experimental data with the theory derived in Chap. 2 using the bubble distribution measured in Chap. 4. We find that the agreement is not that good. Better agreement is obtained with a Gaussian bubble distribution with parameters that were empirically chosen.

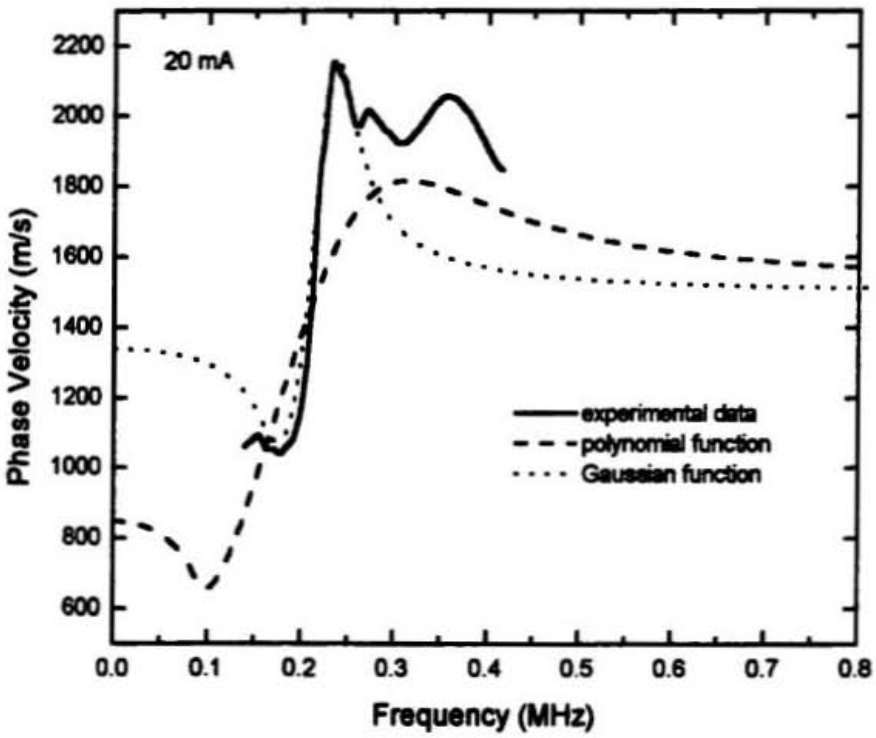

Figure: 5.12

The phase velocity data compared with theory using two different bubble size distribution functions.

In Fig. 5.12, we show the experimental data for the 20 mA sample. Also shown in the figure is a theoretical line calculated for the polynomial fit to the measured distribution. This curve does not match our experimental data very well. We found a better fit using a Gaussian distribution with variables that were empirically chosen. The distribution that fits the data is narrower than the measured distribution. In addition, the mean bubble radius of the measured distribution is 18 μm, is slightly larger than the 14.4 μm mean radius of the Gaussian distribution. We compare the narrow Gaussian distribution with the histogram determined from the image analysis in Fig. 5.13. The mean, standard deviation, and the height of the Gaussian were chosen by hand to give a good fit to the phase velocity data for a given current. We then used the same parameters to calculate the group velocity and attenuation.

Roughly speaking, adjusting the mean bubble size shifts the resonant frequency, which is approximately where the phase velocity changes from less than to greater then the velocity in the bubble free liquid. The width of the distribution changes how abruptly the phase velocity increases with frequency. A narrow distribution gives a steep change in phase velocity with frequency. Finally, the bubble concentration (proportional to the height of the Gaussian) was adjusted to give a good fit to our experimental data. A small bubble concentration leads to small variations in velocity as a function of frequency. Conversely, a large concentration results in very large changes in the velocity. The resulting fits to the phase velocity data for 15 and 20 mA currents are shown in Fig. 5.14.

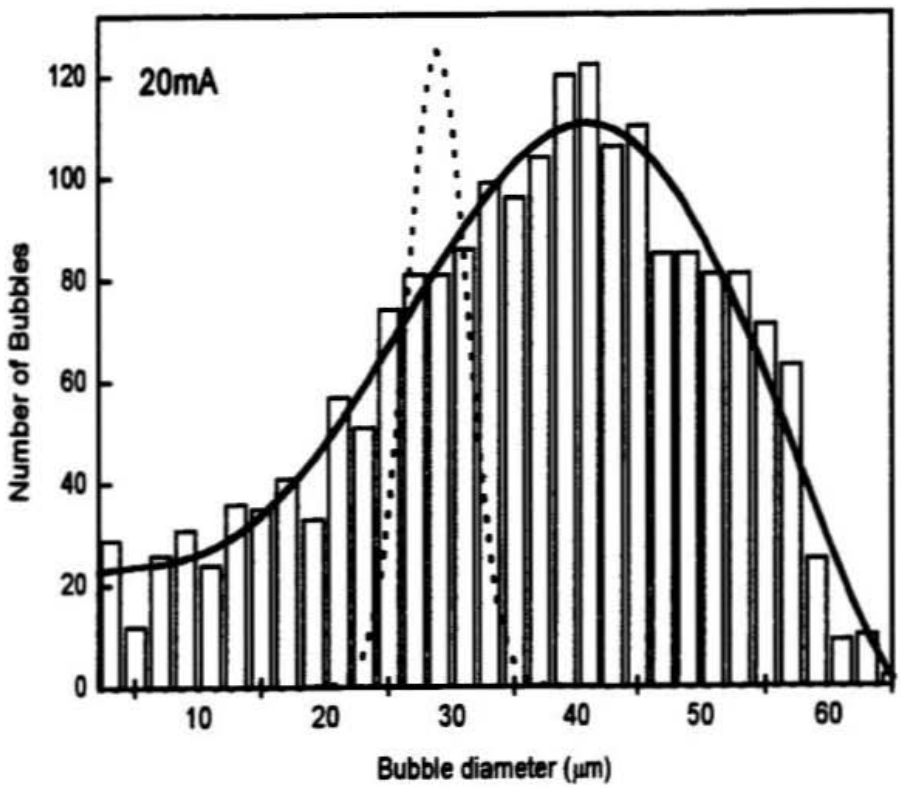

Figure: 5.13

The histogram is the bubble size distribution determined at 20mA with image analysis. The solid line is a polynomial fit to the histogram. The dotted line is the Gaussian size distribution that was used to calculate the dotted line in Fig 5.12. The narrow Gaussian distribution gives a much better fit to the data.

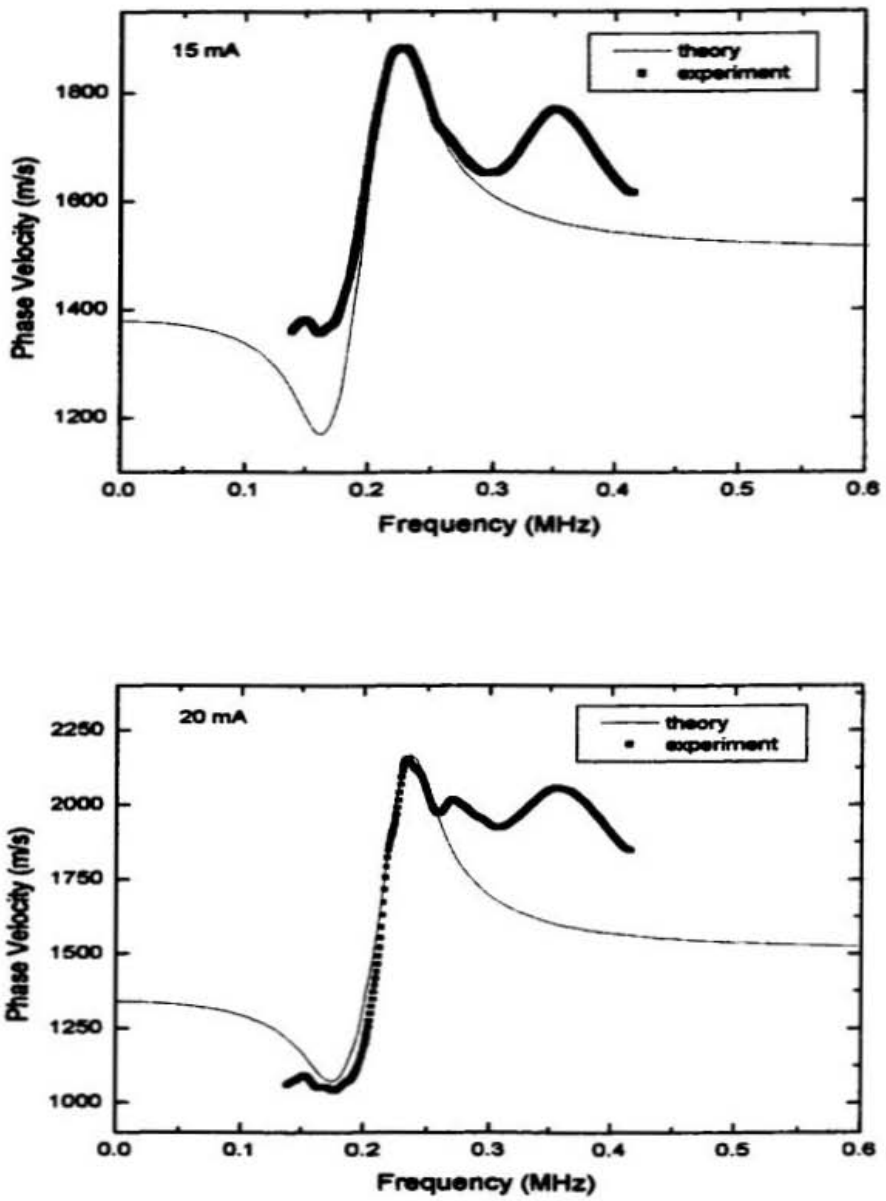

Figure: 5.14

The experimental phase velocities for 15 and 20 mA compared to theory using the Gaussian size distribution discussed in the text.

The agreement between theory and experiment is quite good when using the Gaussian distributions, especially near resonance. However, we see some disagreement at higher frequencies, again near 0.33 MHz. This again is believed to be the result of multiple reflections between the cell walls. Our data for the 20 mA sample also has another fluctuation at 0.27 MHz. We believe that this was the result of some ringing that occured in the transducer during the experiment. Unfortunately, this cannot be confirmed without further experimental work. The Gaussian parameters used are given in Table 5.1.

The experimental group velocity data is compared with the theoretical model in Fig. 5.15. Both the theoretical curve and the experimental data show negative group velocity near resonance. As with the phase velocity, the group velocity curve has a typical shape as a function of frequency, due to the effects of dispersion. There are sharp changes in the group velocity on either side of the resonant frequency where the V_g becomes infinite then negative. There are some disagreements in the data. These occur at the same places as was found in the phase velocity data and are likely of the same cause.

In Fig. 5.16, the attenuation data at currents of 15 and 20 mA are compared to the attenuation calculated using Eq. (2.44). Again, the same parameters for the Gaussian bubble size distributions are used. The comparison between the measured and the calculated attenuation coefficient is quite good for the 15 mA sample, aside from the discussed increase in attenuation at ~0.33 MHz. At a higher void fraction (current = 20 mA) the theoretical attenuation is significantly smaller than the measured attenuation.

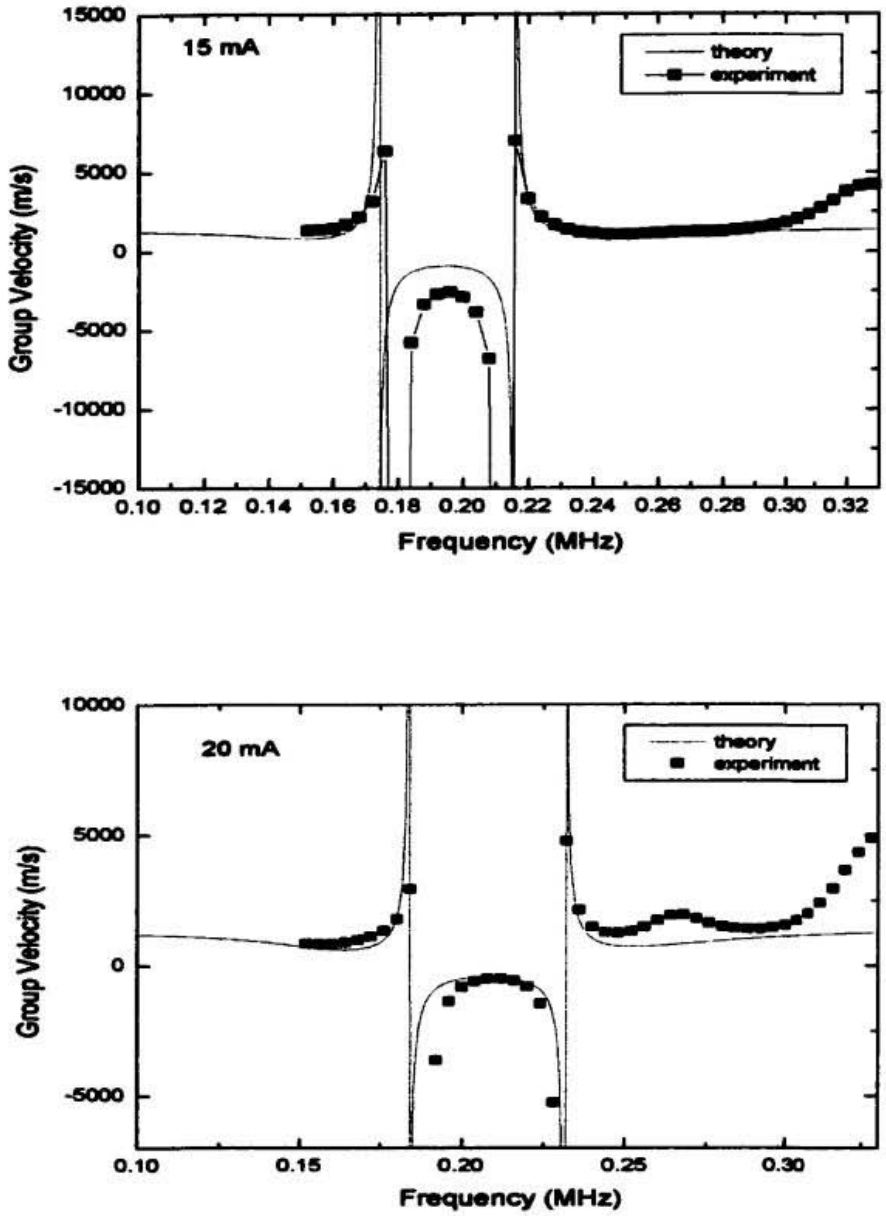

Figure: 5.15

The group velocity data fit to the theoretical model used for void fractions of 15 and 20 mA.

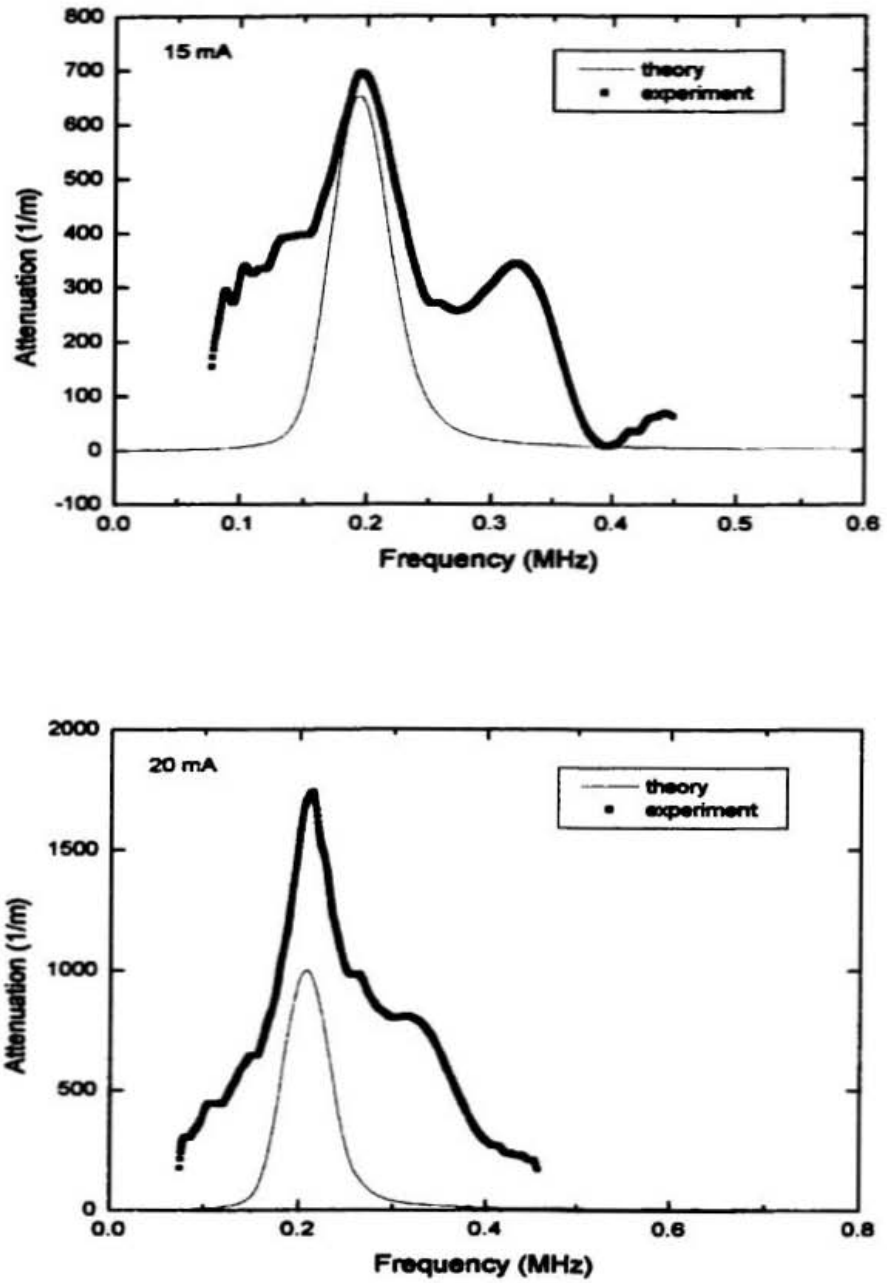

Figure: 5.16

The attenuation data compared to theoretical curves for two different void fractions, using 15 and 20 mA.

Since the Gaussian distribution gives very good agreement with the phase and group velocity data, these results suggest there is some additional attenuation at higher void fractions that is not accounted for in the calculations.

It is obvious that there is some disagreement between the bubble size distribution determined from image analysis, and that which gives good agreement with the data. The bubble distribution changed slightly from day to day. However, the changes recorded from day to day can not account for the very large difference between the two bubble distributions. If the theory is correct, we have made some error in determining the bubble distribution using image analysis. On the other hand, the disagreement with theory may be due to problems with the theoretical model itself. At this time it seems most likely that the error is in the measured bubble distribution. The theory is well established, and some questions arose during the image analysis. The very small bubbles that were detected may not actually be bubbles, but rather small pieces of dust or other foreign debris. The thresholding of the images may lead to a systematic increase in apparent bubble size that would affect the results that were obtained. These two factors could have broadened our measured distribution. Unfortunately, we have no way of checking this without redoing the experiments.

Current (mA)	Gaussian fit to bubble distribution $Gauss(r) = A\exp\left(\frac{-2(r-r_c)^2}{w^2}\right)$		Void fraction used
	w (microns)	r_c (microns)	ϕ (parts per million)
10	3	15	2.2
15	3	15.2	8.6
20	2.4	14.4	12

Table: 5.1

The parameters for the Gaussian bubble size distribution used in the theoretical calculations.

6 Summary

In this thesis, we studied how the propagation of an ultrasonic pulse is affected by a bubbly medium. By adjusting the electric current supplied to our sample cell, we could change the bubble concentration. We studied the attenuation, phase velocity, and group velocity over a range of frequencies. The measurements were then compared with a theoretical model [12]. The bubble size distribution was determined from image analysis. However, the measured distribution did not give good agreement with the theory implying some difficulties with our image analysis. The images used covered a much smaller region than that used for the ultrasonic measurements. As a result we set our image data aside and used a Gaussian distribution, with parameters that were empirically found, for the theoretical calculations. In this chapter, we summarize the work done in this thesis, and suggest possible future work that could augment our current measurements.

We followed Prosperetti's model [6, 12] based on the damped harmonic oscillator, which assumes small linear oscillations of the pulsating bubble. Using this model, we could calculate the thermal, viscous, and radiative damping, as well as the resonant frequency of the bubble. The damping terms could be used to gain an understanding of the scattering and absorption in the bubbly medium via the acoustic cross-sections [12]. The complex wave vector for propagation in the bubbly medium was also calculated. The imaginary part yielded the attenuation, and the real part gave us the phase velocity in the medium. From this we could calculate the group velocity.

The scattering medium, as mentioned, was made up of small bubbles in a liquid. The bubbles were generated using hydrolysis; the oxygen bubbles were guided away and the hydrogen bubbles guided towards the analysis area. The hydrogen bubbles were on average smaller in diameter and were produced at double the rate of the oxygen bubbles. We also found using our theoretical model that the hydrogen gave a high absorption to scattering ratio. We used image analysis software [15] to measure the bubble size distribution and bubble concentrations (or void fractions). Although approximately 1000 bubbles were counted at each concentration we found that using a Gaussian bubble distribution with empirically determined parameters gave a closer match between experiment and theory. At this time, we do not believe there is a problem with the theoretical model used, but rather, a problem with the measured bubble size distribution. We make this conclusion based on two strong considerations: a well established theoretical model and some possible problems with the image analysis recognized in retrospect. It is possible that the pictures taken also contained dirt and other very small contaminants (<4 microns in radius). These tiny particles would have very different effects on the ultrasonic pulses than bubbles would have. Therefore, the apparent bubble size distribution found in the image analysis would be different from what the ultrasonic pulses measured.

The highly absorptive nature of the medium at resonance led to anomalous dispersion. A great deal of attention has been paid to this phenomenon [20]. Because of pulse distortion, anomalously dispersive media have negative or superluminal group velocities. We emphasize that this is not a violation of causality: information cannot

travel faster than light. Under such conditions, information (or energy) does not travel at the group velocity, and we must use other forms of velocity [11, 21] to measure information transfer speed in this regime [2, 4, 5]. Until recently, there has not been good experimental data on negative or superluminal group velocities. In the last few years negative group velocities have been experimentally measured using optical (electromagnetic) waves [8, 9, 23]. We believe this is the first detailed observation of negative group velocity using ultrasonic (acoustic) waves in fluid media.

In the future, we would like to measure the energy velocity for the same medium. The energy velocity can be obtained from measurements of diffusive wave propagation in strongly scattering media. The diffusion constant is defined as

$$D = \frac{v_e l^*}{3}, \tag{6.1}$$

where v_e is the energy velocity and l^* is the transport mean free path. The quantity l^* can be obtained from continuous wave experiments [24]. The diffusion coefficient can be measured using pulsed wave experiments. Knowing these quantities, the energy velocity can be determined. We would like to compare these measurements to for the group velocity, and measurements on light waves. Furthermore, we would like to understand better how to efficiently send and measure information within an anomalous dispersive regime.

References

1 J. H. Page, P. Sheng, H. P. Schriemer, I. Jones, X. Jing, D. A. Weitz, Science (U. K.) **271**, 634 (1996).

2 L. Brillouin, *Wave Propagation and Group Velocity* (Academic Press, New York, 1960).

3 L. Brillouin, *Wave Propagation in Periodic Structures; Electric Filters and Crystal Lattices* (McGraw-Hill, New York, 1946).

4 J. D. Jackson, *Classical Electrodynamics* (Wiley, New York, 1975).

5 L. D. Landau, E. M. Lifshittz, and L. P. Pitaevski, *Electrodynamics of Continuous Media* (Pergamon, Oxford, 1984).

6 A. Prosperetti, J. Acoust. Soc. Am. **61**, 17 (1977).

7 F. E. Fox, S. R. Curley, and G. S. Larson, J. Acoust. Soc. Am. **27**, 534 (1955).

8 L. J. Wang, A. Kuzmich, and A. Dogariu, Nature (U. K.) **406**, 277 (2000).

9 D. Mugnai, A. Ranfagni, and R. Ruggeri, Phys. Rev. Lett. **84**, 4830 (2000).

10 J. Wolf, T. D. K. Ngoc, R. Kille, W. G. Mayer, J. Acoust. Soc. Am. **83**, 122 (1987).

11 K. E. Oughstun and C. M. Balictisis, Phys. Rev. Lett. **77**, 2210 (1996).

12 T. G. Leighton, *The Acoustic Bubble* (Academic Press, San Diego, 1994).

13 L. Landau and E. Lifshitz, *Fluid Mechanics* (Addison-Wesley, Reading, Massachusetts, 1959).

14 C. S. Clay and H. Medwin, *Acoustical Oceanography* (John Wiley & Sons, 1977).

15 Scion Imaging, (Scion Corporation, USA, 2000).

16 S. E. Burns, S. Yiacoumi, and C. Tsouris, Separation and Purification Technology **11**, 221 (1997).

17 D. R. Ketkar, R. Mallikarjunan, and S. Venkatachalam, International Journal of Mineral Processing **31**, 127 (1991).

18 P. Sheng, *Introduction to Wave Scattering, Localization, and Mesoscopic Phenomena* (Academic Press, San Diego, 1995).

19 H. P. Schriemer, PhD thesis (University of Manitoba, Winnipeg, 1997).

20 E. Sonnenschein, I. Rutkevich, and D. Censor, Physical Review E **57**, 57 (1998).

21 G. D'Aguanno, M. Centini, M. Scalora, Physical Review E **63**, 036610 (2001).

22 L. J. Wang, A. Kuzmich, and A. Dogariu, Nature (U. K.) **406**, 277 (2000).

23 M. Mojahedi, E. Schamiloglu, F. Hegeler, K. J. Malloy, Physical Review E **62**, 5758 (2000).

24 H. P. Schriemer, M. L. Cowan, J. H. Page, P. Sheng, Z. Liu, D. A. Weitz, Phys. Rev. Lett. **79**, 3166 (1997).